

POWER MANAGEMENT AND CONTROL OF A GRID- CONNECTED DFIG BASED WIND TURBINE/PV/BATTERY HYBRID RENEWABLE ENERGY SYSTEM

OTHMANI Mohammed*^a and LAMCHICH My Tahar^a

^aFaculty Of Science Semlalia Of Marrakech, Cadi Ayad University, Marrakesh, Morocco

Corresponding author: othmani.mohamed.mmed@gmail.com

ABSTRACT: Three novels Energy Management Strategies (EMSs) are proposed in this paper. These EMSs supervise the control of a Grid-Connected Hybrid Renewable Energy System (GCHRES). The GCHRES describes a Renewable Energy Source (RES) based on Photovoltaic Generator (PVG) and a DFIG based Wind Turbine, associated with a Battery-Based Storage System. PVG, DFIG Rotor and the battery are tied to the Common Coupling Point (CCP) via a reversible three-phase inverter associated with an RL filter, while DFIG Stator is directly connected to the CCP.

The CCP combines the Utility Grid (UG) and a house considered as an AC load, supplied primarily by the mean of RES. The UG supports the RES in case of power generation deficit. Battery is designed to perform peak shaving application in order to avoid the UG subscription power exceeding. Due to the weakness of the battery device, all EMSs aim to ensure continuity of supplying the house, while preserving the battery from over-charges and high depth of discharges. Consequently, reducing of its lifespan would be avoided. Furthermore, the proposed EMSs aim also to reduce the monthly UG customer energy bill. These EMSs differ according on the type of metering with the UG. Energy balance into the system is ensured by controlling RES generation and the battery powers, in addition to the power exchange between the inverter and the UG. Simulation into MATLAB/SIMULINK was used to prove the performances of the GCHRES, in different metering cases, and under several operation modes. Real solar irradiation, temperature and wind speed profiles data of the region of Marrakech in Morocco, were adopted. Results in terms of demand meeting, power supply reliability, global system stability and power references tracking, DC-Bus voltage regulation, are presented in this paper.

Keywords: Energy Management Strategies, Grid-Connected Renewable Energy System, Peak Shaving, Power Flows Control

I. INTRODUCTION

Electric generation from Renewable Energy Sources (RES) is increasing worldwide according to data registered by international agencies such as World Wind Energy Association (WWEA) and International Renewable Energy Agency (IRENA) [1]. In fact, nowadays, the permanent increase of energy demand causes an energy crisis due to the depletion of fossil energy sources. Consequently, electricity price from centralized generation increases as well. Adding to that the environmental deterioration due to Greenhouse Gases emission, and also the energy control technological development, made the integration of RES more attractive. Solar and wind powers, which are clean and abundantly available resources, and which fall under the scope of Decentralized-Generation, are currently widely exploited, and can be used either in autonomous or Grid-connected modes.

PV systems can provide enough power if properly operated, and their performances are better in high solar irradiation areas. But the output power of PVGs is affected, due to the intermittency of climatic conditions. In fact, the power delivered by PVGs depends on the voltage imposed on their terminals. On the Voltage-Power curve, the Maximum Power Point (MPP) must be reached for any solar irradiation and temperature values, in order to take advantage of the fully potential of PVGs. For this purpose, Maximum Power Point Tracking (MPPT) algorithms have been developed. According to a complexity/performance compromise, development of MPPT algorithms had been subject of several works, among which stand out [2 - 5]. These algorithms can be grouped in two families: Firstly, those based on PVG output power derivation such as Incremental Conductance (INC). Secondly, those based on PVG output voltage/current feedback such as the Perturb and Observe (P&O) [6]. [7] Presents a dynamic and speed comparison of different MPPT algorithms. Due to its simple implementation and good performances, P&O due is

considered as the most commonly used MPPT algorithm control for PVGs [8, 9].

The maturity and ease of installation of wind turbines make the evolution of this electricity production system faster, and the recent development in wind power control technology has opened the path for utilizing this power generation system for distributed generation to meet the grid demand. The most important part of this system is the nacelle which contains the generator. Depending on the application and the power generated, the latter can be a direct current machine, a synchronous machine, a singly or doubly fed induction machine (DFIG). In the recent past, the use of the DFIG increased, due to its special features. In fact, DFIG rotor can operate in both sub-synchronous or super-synchronous speeds and the power converter rating can be reduced to approximately 30% of the rated wind turbine power. As special advantages of the DFIG, it can also be found the independent control of the generated active/reactive powers, the high efficiency and reduced mechanical stress on the wind turbine [10]. As for PVG systems, but this time on the Power-Speed curve, the MPP must be reached for any wind speed value, in order to take advantage of the fully potential of the wind turbine. This goal can only be achieved in the case of variable speed wind turbines. The maximum power is reached when the rotor speed follows the wind speed variation to maintain the maximum aerodynamic efficiency of the turbine. Different MPPT methods have been developed for wind turbine systems, and can be classified into three categories. Starting with Tip speed Ratio (TSR), and as presented in [11, 12], this method consists in adjusting the turbine rotational speed to an optimal speed leading to a maximum of the power coefficient. Therefore, rotor and wind speeds must either be measured or estimated. This method can be either with or without speed control. The second method, called Power Signal Feedback (PSF), requires either the Power-Speed or the Torque-Speed characteristics. A

power signal feedback is acquired and nonlinearly mapped to an optimal rotor speed [13, 14]. Finally, the Hill Climb Search (HCS) method constantly search for the MPP and outputs it. This solution operates without any information system and continuously adjusts itself to reach an optimal operating point. The power and/or speed variations are measured periodically. For any given speed reference, if an increase of the power is observed, the direction (sign) of the set point signal remains unchanged and vice versa.

These two systems output powers are highly dependent on weather and intermittent climate conditions. Therefore, perfect services to the grid and to loads requiring a constant power profile, cannot be guaranteed. PVG alone or wind turbine alone cannot lead to satisfactory results. In fact, the primary source of the wind turbine, which is the wind, and that of the PVG, namely solar irradiation, is of different nature in term of time of availability. Thus, Hybridation can be considered as an effective solution, to ensure total power recovery, during the whole day and seasons. A Hybrid Renewable Energy System (HRES) will eliminate the single energy source deficiency, by selecting the best possible advantages of each individual energy source [15]. And in order to improve the performance of the HRES in terms of supply reliability and continuity, the HRES can be Grid-connected or associated with a storage system or even with both simultaneously, to obtain finally a Grid-Connected Hybrid Renewable Energy System (GCHRES). The storage device can be a fuel-cell/electrolyzer association, super-capacitor, flywheel, compressed air, battery bank... and the chosen storage device depends on the application.

As said before, RES can be either autonomous or Grid-Connected which correspond to this paper purpose. Generally, RES power rarely meets demand. Consequently, a power surplus or deficit is often present. Utility Grid (UG) can provide power when RES generation is either zero or unable to satisfy the load demand, which correspond to deficit situations. However, with the increase of the subscription power, the monthly energy bill of UG subscriber increases as well. Therefore, integration of a storage system to perform peak shaving process would be an advantageous application for the UG subscriber. In fact, in many countries, the kWh is more expensive in peak hours, where the energy demand is high. Peak shaving will lead to a reducing in the power requested from the UG, especially during this time period, leading in consequence to a reducing of the UG subscription power and the energy bill as well. It will also be beneficial for eliminating penalties due to the exceeding of subscription power. Peak shaving would be beneficial for both UG and environment also. In fact, less power demand reduces the risks of grid congestion. This will lead to reduce the necessity of backup centralized stations calling. Taking for example the Moroccan case, the kWh production is still very polluting. In fact, 61% of electricity is produced from coal centralized stations [16]. Therefore, as major advantage of peak shaving at the environmental level, less Greenhouse-Gases emissions due to less demand from these stations. [17] Presents a comparison of different storage devices, based on operating power and discharge time, and considers batteries as the most suited for peak shaving applications. However, to increase its lifetime, batteries require accurate regulation of its charge/discharge

currents within manufacturer specified range. Adding to that the State of Charge (SOC) constraints, in fact the latter must be kept in a recommended range. Harmful irreversible reactions in the battery electrodes will be avoided, and hence decreasing battery lifespan will be avoided as well. It is essential to size properly the battery in order to get operational for peak shaving, as soon as the power requested from UG reaches its maximum allowed (subscription power). [18] Presents a battery based Peak shaving application in France, in a system that contains only PVG as RES. In this paper, peak shaving will be studied for GCHRES containing both PVG and a DFIG based Wind turbine as RES.

Connection with the grid can be realized through different metering solution. In this paper, the difference between these metering cases was the first point taken into account in the development of the proposed Energy Management Strategies (EMSs). For example, Fig. 1 shows the metering cases for Grid-connected PVG systems, in self-consumption mode, adopted in Morocco. These metering solutions will constitute the basis of the development of EMSs presented in this paper. For all metering cases, if RES production is either zero or insufficient to meet demand, the UG acts as a backup and the metering index increases, giving the consumed energy to the distributor. Contrarily, when RES power exceeds the one requested, the metering index works according to the three metering types:

Digital Metering (DM in Fig. 1(a)): The metering index increases when the power is injected into UG as if the subscriber has consumed this injected energy (it is the case of around 1 million Moroccan UG subscribers) [19].

Irreversible Electromechanical Metering (IEM in Fig. 1(b)): The metering index does not change when the power is injected into the UG, because of the impossibility of the disc rotation in the opposite direction. In consequence, when injected, energy is consumed in the neighborhood for free.

Reversible Electromechanical Metering (REM in Fig. 1(c)): The meter index will subtract the injected energy due to the possibility of rotation of the disc in the opposite direction. It is clear that this metering solution is the most favorable for the UG subscriber.

Battery integration aiming to perform peak shaving, for the different metering cases presented in Fig. 1, will be studied in this paper, through managing the flow of powers within the GCHRES. This study deals with self-consumption mode (opposite of total sale mode) with net-metering; 1kWh given for one 1kWh delivered [19]. Thus, RES energy selling and UG energy buying prices are not taken into account in the development of this paper EMSs. This economical aspect can be introduced to complete this work in future article, considering also peak and normal hours. As said before, three EMSs are proposed, depending on the metering type solution and on the UG power injection limitation modes. Their common main objective is to ensure continuous supply to the house (AC load). The charge and discharge of the battery will be realized while respecting its technical constraints, related to its maximum charging/discharging powers and to its SOC. The first EMS (EMS 1) concerns a GCHRES equipped with either reversible or irreversible electromechanical meter, in no power injection limitation into the UG. Therefore, the RES are operating globally under the control of their respective MPPT

algorithm. The second EMS (EMS 2) is dedicated for a GCHRES with same metering types as for EMS1, but with grid injection limitation. The output powers of RES are limited in certain cases. PVG power is limited by the mean of a limited power point tracking algorithm, called LPPT and presented in [20]. [21] Presents different LPPT control schemes. EMS1 and EMS2 are combined in one flowchart as will be presented in next sections. The third EMS (EMS 3) is concerning digital metering case, where the subscriber is suffering financial losses when injecting power into UG. Consequently, injection should be avoided at all cost. RES output power is limited in certain cases. The following sections describe these three EMSs in detail. The performances of the proposed GCHRES, under the supervision of each one of these EMSs, are simulated in MATLAB/SIMULINK, based on real weather data (Solar irradiation, temperature and wind speed) of the region of Marrakech in Morocco.

The structure of this paper is as follow: section II describes the proposed GCHRES and the control of each one of its different devices. Section III depicts the method used in the battery sizing, and the proposed EMSs. Section IV shows and discusses the simulation results. Finally, in section V, the results obtained are summarized in a conclusion.

II. SYSTEM MODELLING AND CONTROL

Fig. 3 Illustrates the Proposed GCHRES, Which is two buses based architecture (DC and AC buses). Renewable energy sources constituted of a Solar Generator (PVG) and a DFIG based Wind turbine are considered as the main power sources intended to meet the variable house power demand.

The UG is considered as the main backup energy source in the event of RES power deficit. A battery performs the peak shaving application. PVG and battery are connected to the DC-Bus through their respective power converters. In the same way, the rotor of the DFIG is connected to this bus via a power converter, while the stator is directly connected to the CCP. As the DC-Bus voltage is higher than the voltage variation range of the PVG, a DC-DC Boost converter is necessary for the interfacing between these two elements. The battery voltage can be kept lower than the DC-Bus Voltage, by means of a bidirectional DC/DC Buck-Boost Converter (BBDC). Buck mode operates during the charge and the Boost mode during the discharge. An IGBT based Three Phase converter called Rotor Side Converter (RSC), allows the bidirectional flowing of the power between the rotor of the

DFIG and the DC-Bus, thus allowing both sub-synchronous and hyper-synchronous operations of the machine. The connection between the DC-Bus output and the CCP, combining the UG and the AC-house, is realized via an IGBT based three-phase inverter called Alternative Side Converter (ASC). State-based supervisory controls the power flows within the GCHRES. All devices powers in this article are presented according to the power convention signs of MATLAB/SIMULINK. All correctors presented in this article are Proportional-Integrator (PI) based.

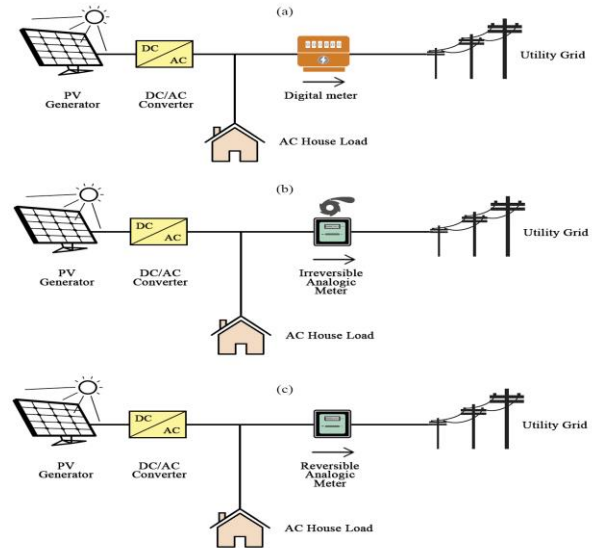


Fig. 1: Metering solution for Grid-Connected solar systems in Morocco (a) DM (b) IEM (c) REM

A. Solar Generator Mathematical Modelling

The single diode model of a PV cell is represented in Fig. 2, which is considered as the most commonly used one [22].

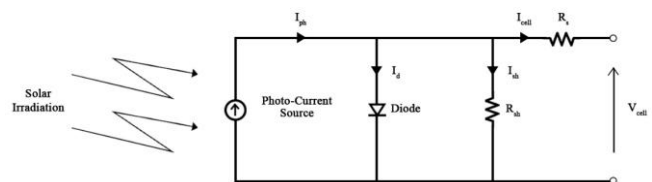


Fig. 2: Single diode representation of PV cell

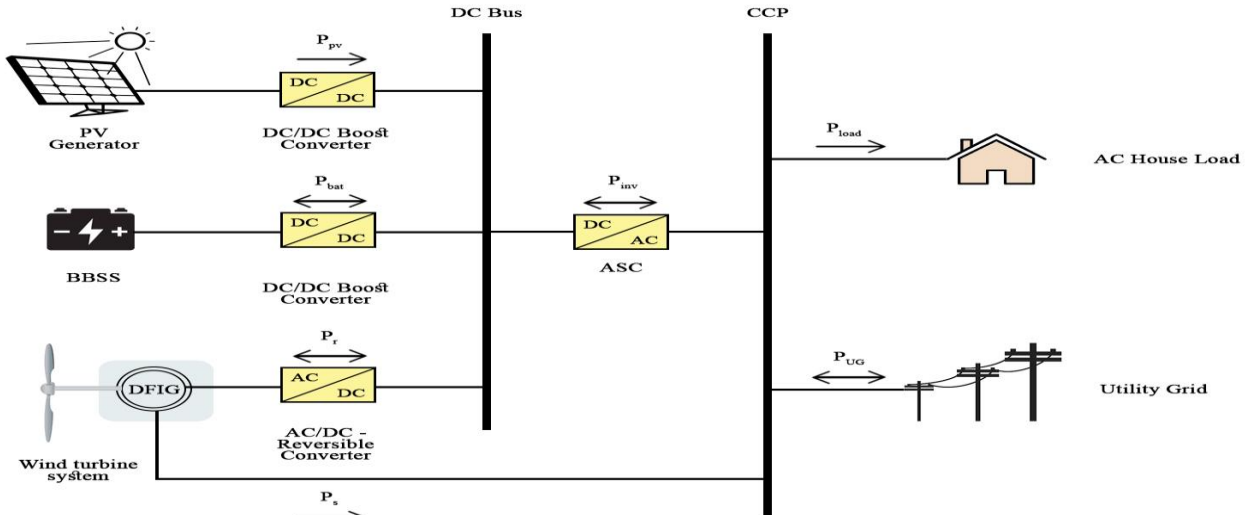


Fig. 3: Architecture of the proposed GCHRES

The single diode model equations are presented below, where all parameters are represented in Tab. 1.

$$I_{cell} = I_{ph} - I_d - I_{sh} \quad (1)$$

$$I_{ph} = [I_{sc} + K_T \cdot (T_c - T_{cref})] \cdot \frac{G}{G_{ref}} \quad (2)$$

$$I_d = I_s \cdot [e^{\frac{q \cdot (V_{cell} + R_s \cdot I_{cell})}{K \cdot T_c \cdot A}} - 1] \quad (3)$$

$$I_s = I_{rs} \cdot \left(\frac{T_c}{T_{ref}}\right)^3 \cdot e^{\frac{q \cdot E_g \cdot (\frac{1}{T_{ref}} - \frac{1}{T_c})}{K \cdot A}} \quad (4)$$

$$I_{rs} = \frac{I_{sc}}{e^{\frac{q \cdot V_{oc}}{K \cdot N_s \cdot A \cdot T_c} - 1}} \quad (5)$$

Tab. 1: PV cell parameters

I_{cell} [A]	PV cell output current
I_{ph} [A]	Photo-current
I_{sh} [A]	Shunt Resistance current
I_d [A]	Diode current
I_s [A]	Reverse Saturation Current of the diode
I_{sc} [A]	Short-Circuit current of the cell under STC
I_{rs} [A]	Diode reverse Saturation Current under STC
K_T [A/K]	Temperature coefficient of the short-circuit current
T_c [C]	Temperature of the cell
T_{cref} [C]	Reference Temperature of the cell
G [W/m ²]	Solar Irradiation
G_{ref} [W/m ²]	Reference Solar Irradiation
q [C]	Electron Charge (1.602 x 10 ⁻¹⁹ C)
V_{cell} [V]	Cell Voltage
I_{cell} [A]	Cell Output Current
K [J/K]	Boltzmann Constant (1.38 x 10 ⁻²³ J/K)
A	Cell ideality factor dependent on PV technology
E_g [eV]	Gap energy of the semiconductor used in the cell (1.1eV for Silicon)
V_{oc} [V]	Cell Open Circuit Voltage
N_s	Number of cells connected in series

In STC, the 8kW_p PVG Voltage-Current and Voltage-Power curves, used in this paper, are presented in Fig. 4(a) and Fig. 4(b) in STC.

Equations (6) and (7) show the maximum and nominal DC/DC Boost converter powers respectively [18].

$$P_{Boost}^{max} = P_{PV}^{max} \quad (6)$$

$$P_{Boost}^{nom} = P_{PV}^{max} \cdot 0,9 \quad (7)$$

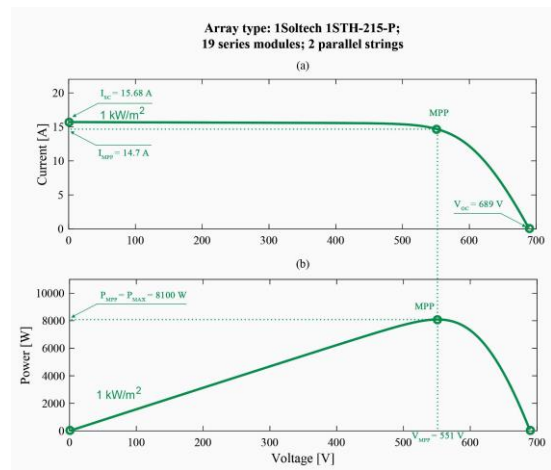


Fig.4: PVG characteristics curves in STC (a) Current-Power (b) Voltage-Power

B. Solar Generator Control

While PVG is turned on (through circuit breaker), it will be controlled by MPPT controls when it's fully potential is requested, otherwise, the LPPT will take over. In both cases, the control algorithm generates at its output the DC/DC Boost converter duty cycle, reaching the desired voltage on the Voltage-Power curve of the PVG. The PWM technique generates the switching signals of the converter IGBTs according to this duty cycle. The PVG overall control

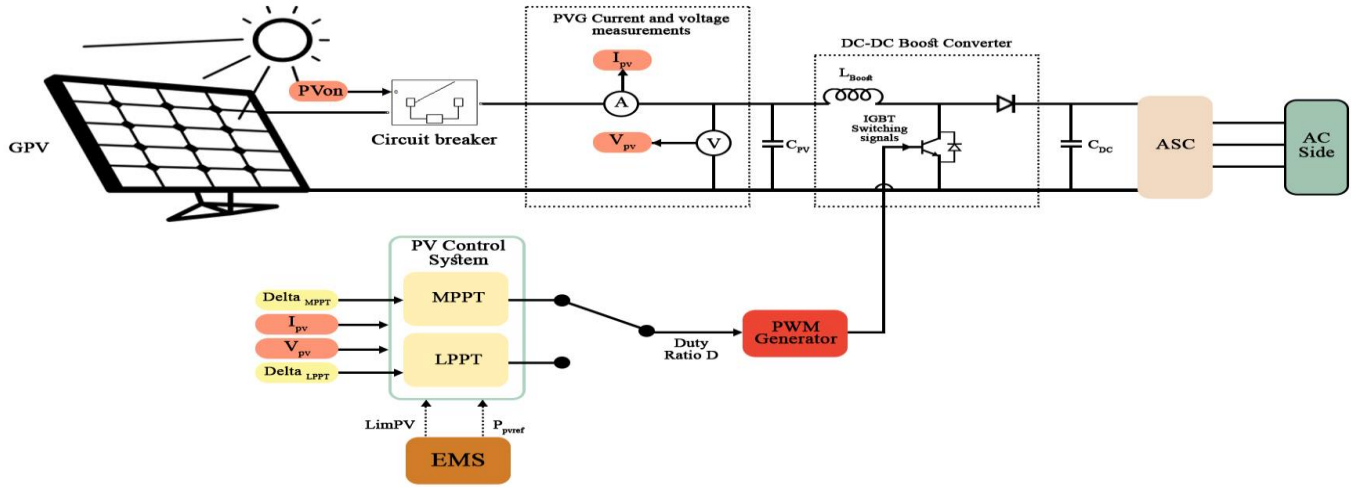


Figure 5: Overall PVG Control architecture

Architecture is depicted in Fig. 5 and Tab. 2 summarizes the parameters of the overall PVG system control used in simulation.

Tab. 2: Simulation overall PVG system characteristics

DC/DC Boost converter control technique	PWM
PV array technology	1Soltech-1STH-215P
PV array peak power	213.1W _p
Number of PV arrays	38
Number of modules in series	19
Number of strings	2
PVG peak Power	8,1kW _p
PVG Open-circuit Voltage	689V
PVG Short-circuit Current	15,68A
PVG MPP-Voltage	551V
PVG MPP-Current	14,7A
DC/DC Boost converter Inductance	1. 10 ⁻⁴ H
DC-Bus Capacity	2,4. 10 ⁻³ F
DC-Bus Voltage	1000V
DC/DC Boost converter nominal power	7.29kW
DC/DC Boost converter maximum power	8,1kW

The point (V_{MPP}, P_{MPP}) is reached by using a P&O control algorithm (right part of Fig. 8), and Fig. 6 depict its operation on the voltage-power curve. When power limitation is required, the supervisory system calculates the PVG reference power according to the EMS in operation. LPPT algorithm (left part of Fig. 8), allows to reach this power. LPPT algorithm makes it possible to reach the limited power point (LPP) on the voltage-power curve, by imposing the corresponding voltage on the PVG terminals. Seen the bell shape of this curve, this power corresponds to two different voltages. It is preferable to impose the highest voltage (corresponding to the right side of the MPP); in order to decrease the PVG output current, allowing the Joule effect losses decrease. LPPT algorithm step Δ_{LPPT} must be reduced when entering the convergence zone (8), thus reducing the amplitude of the oscillations around the power reference P_{pvref} , and thus increasing tracking precision of this reference. Fig. 7 depicts its operation on the voltage-power curve.

$$P_{PV} - P_{PVref} < \varepsilon \tag{8}$$

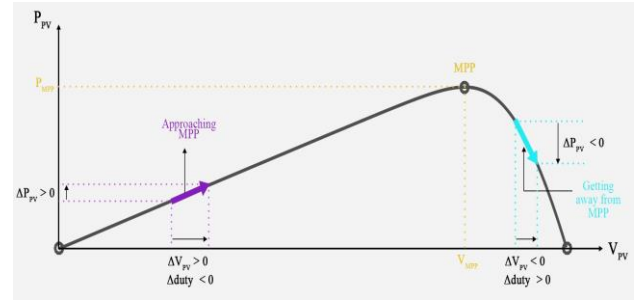


Fig. 6: P&O algorithm principle

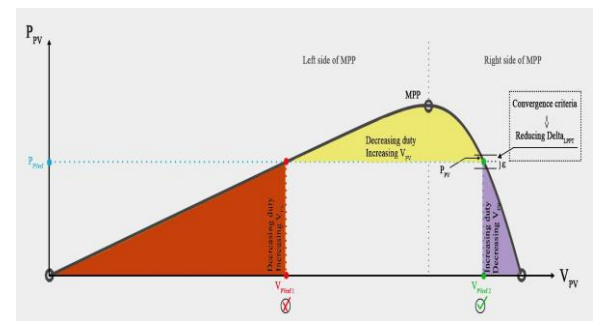


Fig. 7: LPPT algorithm principle

C. Wind System Mathematical Modelling

C.1. Turbine Modelling

The mechanical power captured by the turbine from the wind kinetic power, also called aerodynamic power, is given by (9). The term $C_p(\lambda, \beta)$ represents the turbine power coefficient, function of the TSR λ (10) and the pitch angle β . This coefficient is responsible of the power conversion process losses, and has for maximum value 0.59 known as Betz limit.

$$P_{aero} = \frac{1}{2} C_p(\lambda, \beta) \cdot \rho \cdot \Pi \cdot R^2 \cdot v_{wind}^3 \tag{9}$$

$$\lambda = \frac{\Omega_t \cdot R}{V_{wind}}$$

(10)

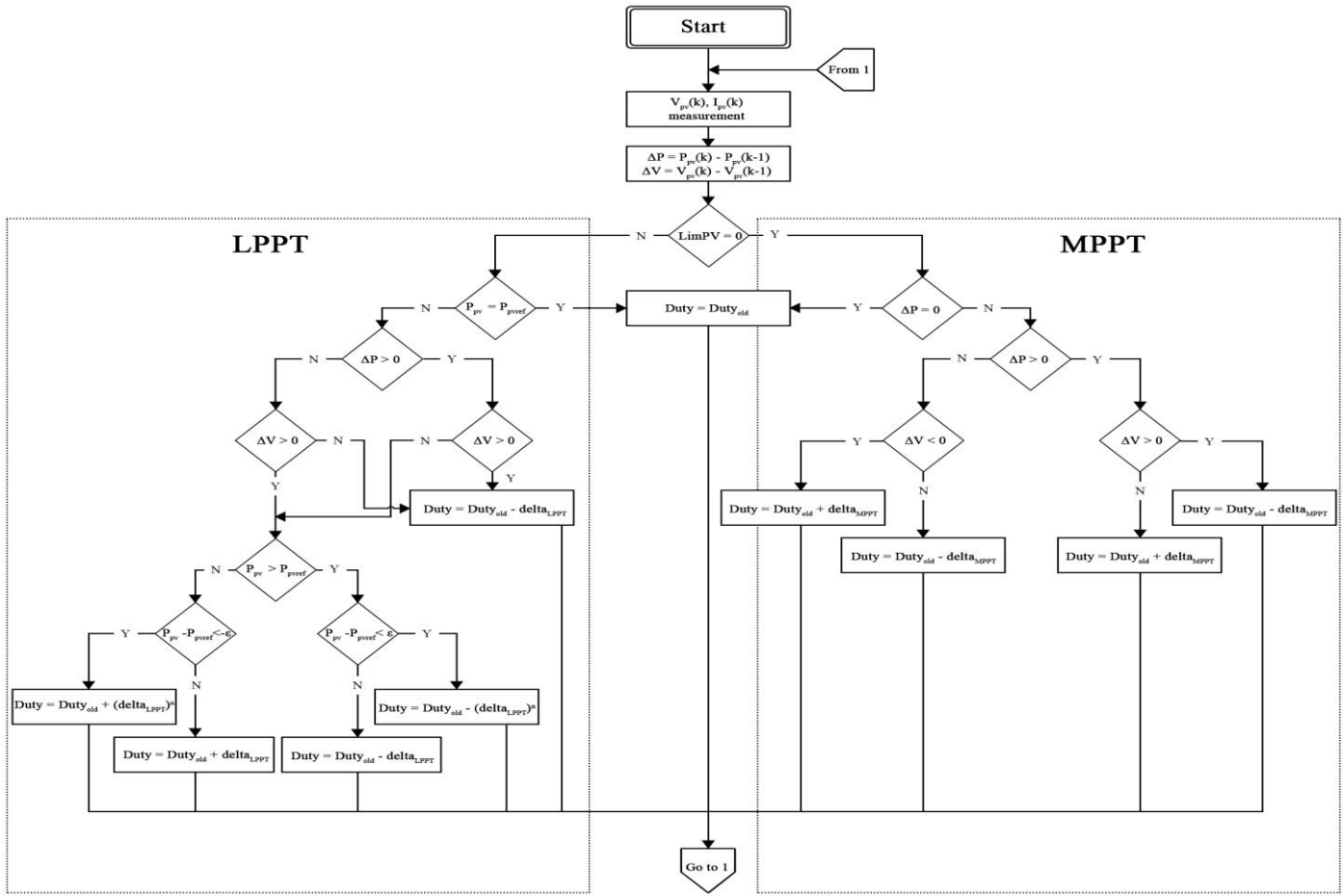


Figure 8: Overall PVG control algorithm

Where: R blade length [m]; V_{wind} Wind speed [m/s]; ρ wind density [kg/m^3]; Ω_t turbine angular speed [rad/s]. The expression of the power coefficient used in this paper is given by (11).

$$C_p(\lambda, \beta) = (0.5 - 0.0167\beta) \cdot \sin\left[\frac{\pi(\lambda+0.1)}{18.5-0.3(\beta)}\right] - 0.00184 \cdot (\lambda - 3)\beta \quad (11)$$

Fig. 9 shows the power coefficient curves function of the TSR, for different pitch angle values. It is clear that the extracted power decreases with pitch angle increases.

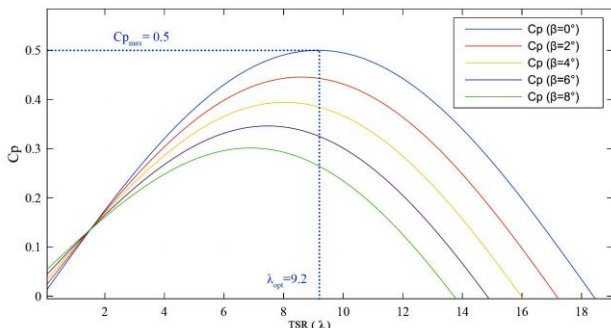


Fig. 9: Power Coefficient of the wind turbine

C.2. DFIG Modelling

The mathematical modelling of the electrical part of the wind turbine system (DFIG) is developed under some of simplifying assumptions [23]. Stator and rotor voltages, in PARK reference frame is given by the equation system (12) and (13) respectively.

$$\begin{pmatrix} v_{sd} \\ v_{sq} \end{pmatrix} = \begin{pmatrix} R_s & 0 \\ 0 & R_s \end{pmatrix} \begin{pmatrix} i_{sd} \\ i_{sq} \end{pmatrix} + \frac{d}{dt} \begin{pmatrix} \varphi_{sd} \\ \varphi_{sq} \end{pmatrix} + \begin{pmatrix} 0 & -\omega_s \\ \omega_s & 0 \end{pmatrix} \begin{pmatrix} \varphi_{sd} \\ \varphi_{sq} \end{pmatrix} \quad (12)$$

$$\begin{pmatrix} v_{rd} \\ v_{rq} \end{pmatrix} = \begin{pmatrix} R_r & 0 \\ 0 & R_r \end{pmatrix} \begin{pmatrix} i_{rd} \\ i_{rq} \end{pmatrix} + \frac{d}{dt} \begin{pmatrix} \varphi_{rd} \\ \varphi_{rq} \end{pmatrix} + \begin{pmatrix} 0 & -\omega_r \\ \omega_r & 0 \end{pmatrix} \begin{pmatrix} \varphi_{rd} \\ \varphi_{rq} \end{pmatrix} \quad (13)$$

Where: $\omega_r = \omega_s - \omega$ rotor voltage/current pulsation [rad/s]; $\omega_s = 2\pi f_s = 2\pi \cdot 50$ stator voltage/current pulsation [rad/s]; $\omega = p\Omega_{mec}$ electrical speed of the DFIG shaft [rad/s]; Ω_{mec} Mechanical speed of the DFIG shaft [rpm]; p number of pole pairs; R_s, R_r respectively stator and rotor winding resistance [Ω]; $\varphi_{sd}, \varphi_{sq}, \varphi_{rd}, \varphi_{rq}$ respectively direct and quadrature components of stator and rotor fluxes [Weber]; $i_{sd}, i_{sq}, i_{rd}, i_{rq}$ respectively direct and quadrature components of stator and rotor currents [A].

Stator and rotor fluxes in PARK reference frame are tied to the current by the equation system (14).

$$\begin{pmatrix} \varphi_{sd} \\ \varphi_{sq} \\ \varphi_{rd} \\ \varphi_{rq} \end{pmatrix} = \begin{pmatrix} L_s & 0 & M & 0 \\ 0 & L_s & 0 & M \\ M & 0 & L_r & 0 \\ 0 & M & 0 & L_r \end{pmatrix} \begin{pmatrix} i_{sd} \\ i_{sq} \\ i_{rd} \\ i_{rq} \end{pmatrix} \quad (14)$$

Where L_s , L_r and M are respectively stator, rotor and leakage inductance [H].

Stator and rotor active and reactive powers are given respectively by (15), (16), (17) and (18).

$$P_s = \frac{3}{2} (v_{sd}i_{sd} + v_{sq}i_{sq}) \quad (15)$$

$$P_r = \frac{3}{2} (v_{rd}i_{rd} + v_{rq}i_{rq}) \quad (16)$$

$$Q_s = \frac{3}{2} (v_{sq}i_{sd} - v_{sd}i_{sq}) \quad (17)$$

$$Q_r = \frac{3}{2} (v_{rq}i_{rd} - v_{rd}i_{rq}) \quad (18)$$

The expression of the electromagnetic torque is shown in (19).

$$C_{em} = \frac{3}{2} p \frac{M}{L_s} (\varphi_{sq}i_{rd} - \varphi_{sd}i_{rq}) \quad (19)$$

D. Wind Turbine System Control

Wind turbine system power can be controlled mechanically by controlling the blades pitch angle, or electrically by controlling the generator speed by mean of electromagnetic torque. The control methodology depends on the operating zone of the wind turbine as shown in Fig. 10. It shows that there are 3 zones of the power control, which differs according to the wind speed. v_s Represents the starting speed, from where wind turbine begins producing energy (zone 1). The second zone (normal wind speed), is delimited by v_s and the nominal speed v_n . In this zone, the power in the generator shaft depends on the wind speed. The system is under an optimal control (MPPT), achieved through DFIG electromagnetic torque control. The third zone is when the wind speed is between v_n and the cut-off speed v_{c_off} (high wind speeds), the power is limited to the nominal power to protect the system from mechanical failures, via controlling the pitch angle of the blades, by Stall technique, or by active stall method. Finally, when the wind speed exceeds v_{c_off} , the system is turned off to ensure operation safety, and no power is produced. This paper deals with the control in zone 2 aiming to reach two main objectives through the RSC:

- Setting rotor direct current to zero ($i_{rdref} = 0$), to minimize rotor current, and therefore reducing the dimensioning of the rotor windings, as well as the RSC.
- Following the electromagnetic torque reference C_{emref} , obtained by the MPPT control, or by power reducing control when wind system power must be limited.

Wind turbine power

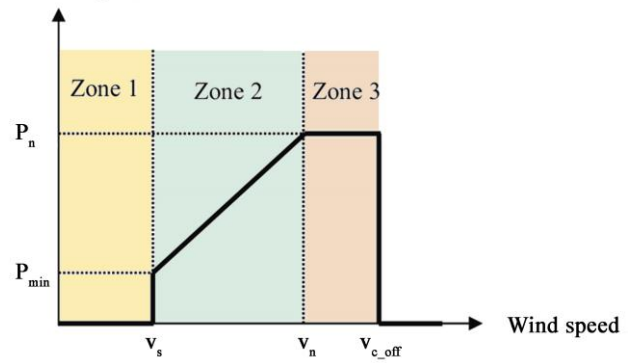


Fig. 10: Operating zones of the wind turbine

By neglecting stator and rotor copper losses, and assuming that there are no conversion losses at the gear box level, the total electrical active power generated by the DFIG is given by (20).

$$P_g = P_s + P_r = C_{em}\Omega_{mec} = P_{aero} = \frac{1}{2} C_p(\lambda, \beta) \cdot \rho \cdot \Pi \cdot R^2 \cdot v_{wind}^3 \quad (20)$$

Where: P_s electrical active power delivered by the stator [W]; P_r electrical active power delivered by the rotor [W]; Equation (20) shows that the control of the DFIG generated power and thus the active power delivered to the CCP, depends on $C_p(\lambda, \beta)$ value. By fixing the pitch angle to its optimal value ($\beta = 0^\circ$), the desired power to be generated is achieved by reaching a specific value of the power coefficient, depending on the operating mode (maximizing/reducing power). This specific value depends only on the TSR that depends on blade length, wind speed and the turbine speed according to (10). Therefore, controlling the wind turbine speed ($\Omega_{turbine}$) leads to control the wind turbine generated power. The relation between the mechanical speed of the DFIG and the turbine speed is given by (21), where G represents the gearbox ratio.

$$\Omega_{mec} = G\Omega_{turbine} \quad (21)$$

The second law of Newton applied to the DFIG shaft is given by (22).

$$J \frac{d\Omega_{mec}}{dt} = C_{mec} = C_t - C_{em} - f_v \Omega_{mec} \quad (22)$$

Where: J Rotor Inertia [Kg.m²]; C_{mec} total mechanical torque on the DFIG shaft [N.m]; C_t torque captured by turbine [N.m]; f_v viscous friction [N].

Thus, by controlling the electromagnetic torque, the mechanical speed of the DFIG shaft is controlled. In consequence, the turbine speed is controlled according to (21), reaching the desired operating point and generated power.

D.1. Maximum Power Point Tracking Mode

The indirect speed control MPPT method is inspired by [24]. Fig. 11 shows the principle of the indirect speed control, with a viscous friction neglecting ($f_v = 0$).

$$P_{aero_max} = \frac{1}{2} C_{pmax} \cdot \rho \cdot \Pi \cdot R^2 \cdot v_{wind}^3 \quad (23)$$

Equation (24) shows the electromagnetic torque reference generated by the MPPT control.

$$C_{em_ref} = -K_{opt} \Omega_{mec}^2 = -\frac{1}{2} \cdot \rho \cdot \Pi \cdot R^5 \frac{C_{pmax}}{\lambda_{opt}^3 G^3} \Omega_{mec}^2 \quad (24)$$

It is clear from Fig. 9 that the maximum power captured by the wind turbine corresponds to a value of the power coefficient equal to $C_{pmax} = 0.5$, corresponding to an optimal TSR equal to $\lambda_{opt} = 9.2$ for a pitch angle equal to 0 degree ($\beta = 0^\circ$).

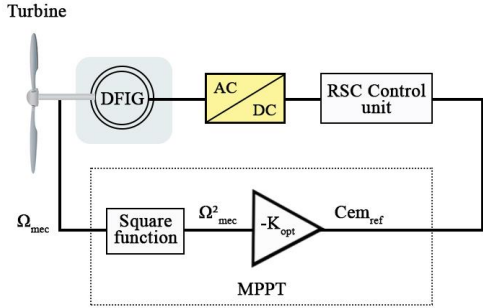


Fig. 11: Indirect Speed Control for Wind Turbine MPPT

D.2. Reduced Power Mode

The wind speed being less than its nominal value, the pitch angle is kept at its optimal value ($\beta = 0^\circ$). The reference power to be generated P_{g_ref} is the desired aerodynamic power to be captured P_{aero_ref} . This power is reached by imposing a reducing power coefficient C_{p_red} , obtained by (25).

$$C_{p_red} = C_p(\lambda_{red}, 0) \quad (25)$$

The reduced turbine speed reference is shown in (26) by resolving (25).

$$\Omega_{turbine_red} = \left[\sin^{-1} \left(\frac{P_{aero_ref}}{\frac{1}{4} \cdot \rho \cdot \Pi \cdot R^2 \cdot v_{wind}^3} \right) \frac{18.5}{\Pi} - 0.1 \right] \frac{v_{wind}}{R} \quad (26)$$

Finally the reduced DFIG mechanical speed reference is obtained (27).

$$\Omega_{mec_red} = G \Omega_{turbine_red} \quad (27)$$

The electromagnetic torque reference is the output of the DFIG speed loop based on PI controller.

D.3. Vector Control of DFIG

The DFIG is controlled through its rotor via the RSC. By choosing a rotating referential frame (dq) linked to the stator rotating flux field, the vector control induces the DFIG model simplifying. Stator fluxes in (dq) frame becomes:

$$\begin{pmatrix} \varphi_{sd} \\ \varphi_{sq} \end{pmatrix} = \begin{pmatrix} \varphi_s \\ 0 \end{pmatrix} \quad (28)$$

And by neglecting stator resistance, stator voltages becomes:

$$\begin{pmatrix} v_{sd} \\ v_{sq} \end{pmatrix} = \begin{pmatrix} 0 \\ \omega_s \varphi_s \end{pmatrix} \quad (29)$$

Where: φ_s the stator flux amplitude [Weber], will be constant because the stator is directly connected to the CCP.

The expression of the electromagnetic torque established in (19) becomes (30), and shows that the latter is controlled only by quadrature component of the rotor current i_{rq} .

$$C_{em} = -\frac{3}{2} p \frac{M}{L_s} \varphi_s i_{rq} \quad (30)$$

Stator reactive power is given by (31) and can be controlled via direct rotor current component i_{rd} .

$$Q_s = -\frac{3}{2} \omega_s \frac{M}{L_s} \varphi_s \left(i_{rd} - \frac{\varphi_s}{M} \right) \quad (31)$$

But as said before, in this article, rotor direct current i_{rd} will be controlled to follow $i_{rdref} = 0$ [25].

Synchronization between the RSC and the CCP is realized by a PLL block (Fig. 12). The connection between the RSC and the CCP requires to continuously determining the phase angle, on which active and reactive powers control depend mainly. Fig. 13 details the overall RSC Control scheme.

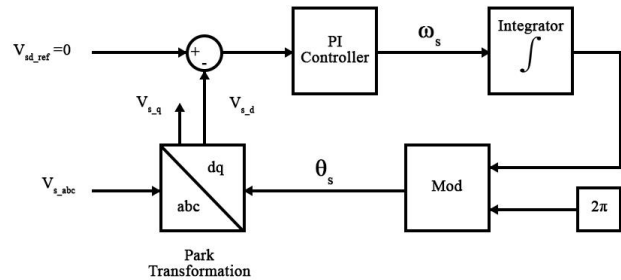


Fig 12: PLL Control Diagram

Equations (32) and (33) show respectively maximum and nominal power of the RSC [18]. This sizing corresponds to a rotor power that not exceeds 35% of the DFIG nominal power. Tab. 3 summarizes the overall Wind turbine system control parameters used in simulation.

$$P_{RSC}^{max} = P_r^{max} = P_{DFIG}^{nom} \cdot 0,35 \quad (32)$$

$$P_{RSC}^{nom} = P_{RSC}^{max} \cdot 0,9 \quad (33)$$

E. Battery Mathematical Modelling

Many models are available in the literature [26 - 30], to meet fine and rapid simulation needs. A Lead-Acid battery is used

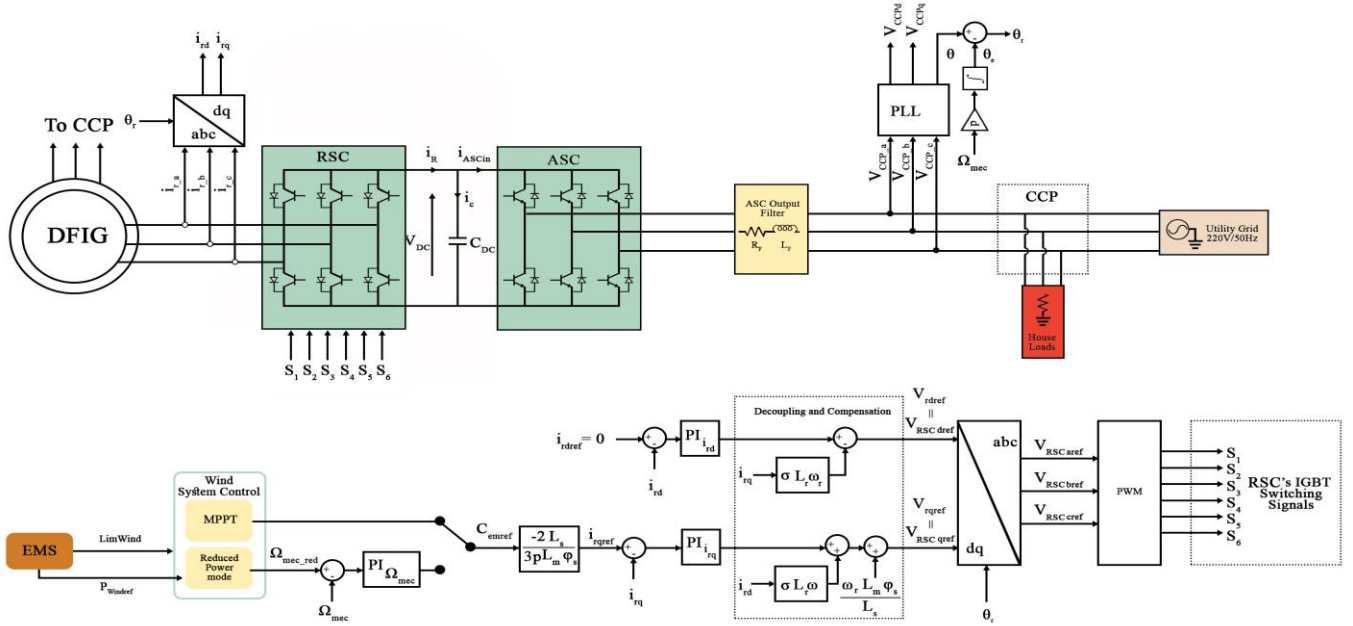


Figure 13: Overall Wind turbine control architecture

in this study's simulation included in the SIMPOWERSYSTEM Toolbox of MATLAB/SIMULINK. The voltage on the battery terminals is given by (34). Open circuit voltage E_{bat} is given during charge and discharge processes by (35) and (36) respectively. According to [31], the instantaneous SOC value is given by (37). Fig. 14 shows the battery equivalent circuit. Tab. 4 resumes the parameters of this model.

$$U_{bat} = E_{bat} - R_{int} i_{bat} \quad (34)$$

$$E_{bat-char} = E_0 - K \cdot \frac{Q}{|i_t| + 0.1Q} \cdot i^* - K \cdot \frac{Q}{Q - i_t} \cdot i_t + F_{hyst-char}(i_{bat}) \quad (35)$$

$$E_{bat-disch} = E_0 - K \cdot \frac{Q}{Q - i_t} \cdot i^* - K \cdot \frac{Q}{Q - i_t} \cdot i_t + F_{hyst-disch}(i_{bat}) \quad (36)$$

$$SOC(\%) = 100 \cdot \left(1 - \frac{\int i_{bat} dt}{Q}\right) \quad (37)$$

Tab. 4: Battery model parameters

U_{bat} [V]	Voltage at the battery terminals
E_{bat} [V]	battery Open-Circuit Voltage
R_{int} [Ω]	battery Internal Resistance
i_{bat} [A]	battery Current
E_0 [V]	Constant Voltage
K	Polarization constant or polarization resistance
i^* [A]	Dynamic Low Frequency current
i_t [A]	Capacity Extracted
Q [C]	Maximum battery Capacity
$F_{hyst-char}(i_{bat})$	battery current Functions representing Hysteresis phenomenon of the battery during charge
$F_{hyst-disch}(i_{bat})$	battery current Functions representing Hysteresis phenomenon of the battery during discharge

Tab. 3: Wind Turbine & RSC control characteristics

Wind Turbine Nominal Power	6.5kW
Number of Pole pairs p	2
Nominal Wind Speed	11m/s
Gear Box Ratio G	5
Blade Length R	2.5m
Friction Factor	0.0023N.m.s
Rotor Inertia	0.0058kg.m ²
Stator resistance	1.06 Ω
Rotor resistance	0.8 Ω
Stator inductance	0.0206H
Rotor inductance	0.01H
Mutual inductance	0.0604H
RSC control technique	PWM
RSC nominal power	2.04kW
RSC maximum power	2.27kW
Proportional Gain of DFIG speed controller	0.116
Integral Gain of DFIG speed controller	1.16
Proportional Gain of i_{rd} PI controller	159.2
Integral Gain of i_{rd} PI controller	177970
Proportional Gain of i_{rq} PI controller	159.2
Integral Gain of i_{rq} PI controller	177970

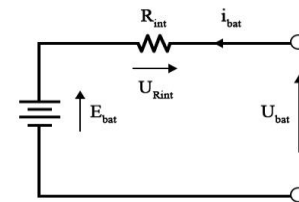


Fig 14: Battery equivalent circuit representation

Maximum and nominal powers of the DC/DC Boost converter are given by equations (38) and (39) respectively [18].

$$P_{Buck-Boost}^{max} = \max(|P_{bat_{ch}}^{max}|, P_{bat_{disch}}^{max}) \quad (38)$$

$$P_{Buck-Boost}^{nom} = P_{Buck-Boost}^{max} \times 0.9 \quad (39)$$

Where $P_{bat_{ch}}^{max}$ and $P_{bat_{disch}}^{max}$ are the battery maximum charging/discharging powers respectively. The battery overall system characteristics used in simulation are presented in Tab. 5, where the complementary information concerning the battery sizing are detailed in section III.

Tab. 5: Simulation overall battery system characteristics

BBDC control technique	PWM
Battery type	Lead Acid
Battery maximum capacity	191Ah
Battery voltage	504V
Battery maximum charging power	-6.8kW
Battery maximum discharging power	5.2kW
BBDC Inductance	5.10^{-2} H
DC-Bus Capacity	$2.4.10^{-3}$ F
DC-Bus Voltage	1000V
BBDC converter nominal power	6.12kW
BBDC maximum power	6.8kW
Proportional Gain of battery PI controller	0.1
Integral Gain of battery PI controller	10

F. Battery Control

The battery reference power P_{batref} to be delivered/received by the battery is generated by the supervisory system. A current control loop control based on PI corrector is used to adjust the battery current at its reference by generating at its output the BBDC duty cycle. The opposite switching signals S_1 and S_2 of the BBDC are generated via PWM technique. The battery overall control process is illustrated in Fig. 15.

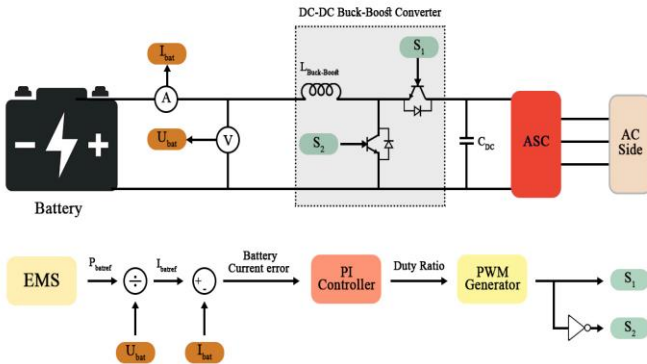


Fig. 15: Overall Battery-Bank control architecture

G. AC Side Equations

The alternative side of the GCHRES is indicated in Fig. 16. Equation systems (40) and (41) represent respectively voltage and current equations.

$$\begin{pmatrix} v_{CCP.a} \\ v_{CCP.b} \\ v_{CCP.c} \end{pmatrix} = \begin{pmatrix} R_F & 0 & 0 \\ 0 & R_F & 0 \\ 0 & 0 & R_F \end{pmatrix} \begin{pmatrix} i_{F.a} \\ i_{F.b} \\ i_{F.c} \end{pmatrix} + \begin{pmatrix} L_F & 0 & 0 \\ 0 & L_F & 0 \\ 0 & 0 & L_F \end{pmatrix} \frac{d}{dt} \begin{pmatrix} i_{F.a} \\ i_{F.b} \\ i_{F.c} \end{pmatrix} + \begin{pmatrix} v_{ASC.a} \\ v_{ASC.b} \\ v_{ASC.c} \end{pmatrix} \quad (40)$$

$$\begin{pmatrix} i_{F.a} \\ i_{F.b} \\ i_{F.c} \end{pmatrix} + \begin{pmatrix} i_{s.a} \\ i_{s.b} \\ i_{s.c} \end{pmatrix} = \begin{pmatrix} i_{L.a} \\ i_{L.b} \\ i_{L.c} \end{pmatrix} + \begin{pmatrix} i_{UG.a} \\ i_{UG.b} \\ i_{UG.c} \end{pmatrix} \quad (41)$$

After PARK transformation, the system (40) is transformed to system (42).

$$\begin{pmatrix} v_{CCPd} \\ v_{CCPq} \end{pmatrix} = \begin{pmatrix} R_F & 0 \\ 0 & R_F \end{pmatrix} \begin{pmatrix} i_d \\ i_q \end{pmatrix} + \begin{pmatrix} L_F & 0 \\ 0 & L_F \end{pmatrix} \frac{d}{dt} \begin{pmatrix} i_d \\ i_q \end{pmatrix} + \begin{pmatrix} 0 & \omega L_F \\ -\omega L_F & 0 \end{pmatrix} \begin{pmatrix} i_d \\ i_q \end{pmatrix} + \begin{pmatrix} v_{ASCd} \\ v_{ASCq} \end{pmatrix} \quad (42)$$

Where: $j = (a, b, c)$; $i_{F,j}$ ASC output filter currents [A]; $i_{s,j}$ DFIG stator currents [A]; $i_{L,j}$ load currents [A]; $i_{UG,j}$ UG currents [A]; $v_{CCP,j}$ simple voltages of CCP [V]; $v_{ASC,j}$ output voltages of ASC [V]; R_F ASC output Filter resistance [Ω]; L_F ASC output Filter inductance [H]; v_{CCPd}, v_{CCPq} respectively direct and quadrature CCP voltage components [V]; v_{ASCd}, v_{ASCq} respectively direct and quadrature ASC output voltage components [V]; i_d, i_q respectively direct and quadrature filter current components [A]; ω Utility Grid current/voltage Pulsation [rad/s].

H. VOC Control of ASC

Two main objectives are reached by controlling the ASC. First, ensuring unity power factor on the AC-side. Secondly, regulating the DC-Bus voltage at its reference value. Keeping the DC-Bus voltage constant is very important since all the power converters are connected to this bus. In fact, large fluctuations of this bus voltage increase the power losses of the power converters and also harmonics injection into the UG. In addition, DC-bus voltage stability influences on the operating performances of the DFIG especially during fault situations. The DC-Bus voltage references and the reactive power reference are fixed to $V_{DCref} = 1000$ V and $Q_{ccpref} = 0$ VAR respectively. Power equations are given by (43) and (44).

$$P_{DC} = V_{DC} \cdot i_c = P_{HS} - P_{ASCin} \quad (43)$$

$$P_{HS} = P_{pv} + P_{bat} + P_r \quad (44)$$

Where: P_{DC} DC-Bus power [W]; P_{ASCin} ASC input power [W]; P_{HS} renewable hybrid system power (without DFIG stator power) [W]; P_{pv} PVG output power [W]; P_{bat} Battery charging/discharging power [W]; P_r DFIG rotor active power [W].

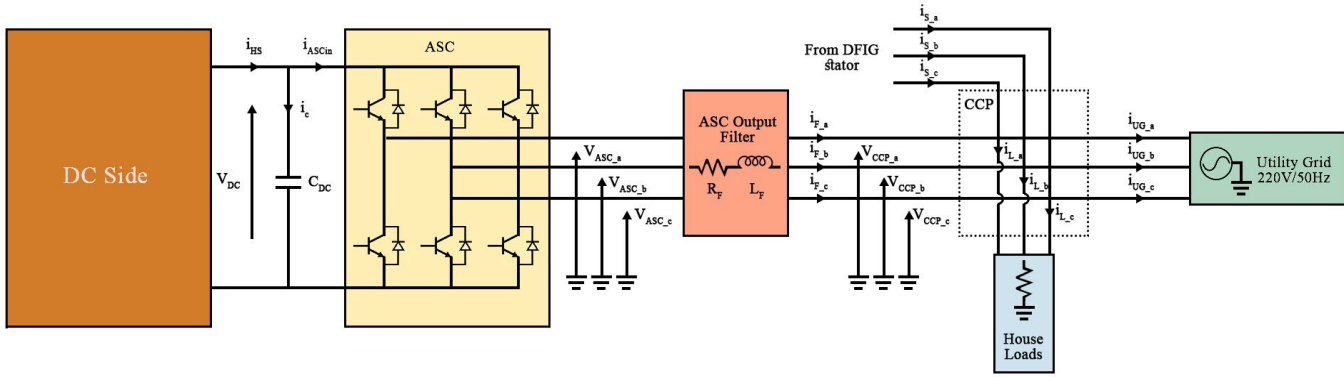


Figure 16: AC-side of the GCHRES

VOC principle consists on aligning the d-axis of the (dq) rotational coordinate system with the CCP voltage direct component v_{pccd} , thus the voltage at the CCP level will be:

$$v_{CCPd} = V_{CCP} \quad (45)$$

$$v_{CCPq} = 0 \quad (46)$$

Neglecting the ASC losses and the filter resistance, CCP active power is given by (47).

$$P_{CCP} = P_{ASCout} = P_{ASCin} = \frac{3}{2} V_{CCP} \cdot i_d \quad (47)$$

Equation (47) shows that the ASC input power can be controlled by controlling only d-axis current i_d , since after the alignment of the v_{CCPd} with the d-axis, this latter became constant. In consequence, the DC-Bus power will also be controlled according to (43). The CCP reactive power is given by (48) and according to (45) and (46), it will also be reduced to (49).

$$Q_{CCP} = \frac{3}{2} (v_{CCPq} \cdot i_d - v_{CCPd} \cdot i_q) \quad (48)$$

$$Q_{CCP} = -\frac{3}{2} V_{CCP} \cdot i_q \quad (49)$$

Consequently, the reactive power exchange between the CCP and the ASC can be controlled by controlling only the q-axis current i_q . Fig. 17 details the overall ASC Control scheme. The synchronization between the ASC and the UG is realized by a PLL block. SVPWM control technique is used to control the ASC in order to reduce current ripples and also the switching frequency of the ASC IGBTs [23]. Maximum and nominal powers of the ASC are shown by equations (50) and (51) respectively [18]. Tab. 6 shows the AC side parameters used in simulation,

$$P_{ASC}^{max} = \max(|P_{bat_{ch}}^{max}|, P_{bat_{disch}}^{max}) + P_{PV}^{max} + P_r^{max} \quad (50)$$

$$P_{ASC}^{nom} = P_{ASC}^{max} \cdot 0,9 \quad (51)$$

Tab. 6: Simulation AC-side characteristics

ASC control technique	SVPWM
ASC output filter resistance	0.3Ω
ASC output filter inductance	5.4 10 ⁻³ H
ASC nominal power	17.17kW
ASC maximum power	15.453kW
Proportional Gain of DC-Bus PI controller	1.096
Integral Gain of battery PI controller	25.35
Proportional Gain of I_d PI controller	11.7
Integral Gain of I_d PI controller	4687.1
Proportional Gain of I_q PI controller	11.7
Integral Gain of I_q PI controller	4687.5

III. BATTERY SIZING AND EMSS

A. Battery Sizing for Peak Shaving Application

To size the battery correctly, monthly real average data of solar irradiation and temperature of the region of Marrakech have been collected from [32]. Average wind speed data were collected from [33] Appendix A shows these data. Monthly average estimation of the demand profile, on hourly basis, has been also required. The battery operates to perform peak shaving application, as mentioned above. Therefore, the latter is sized according to the following criteria: maximum charging power, maximum discharging power, daily energy to be absorbed and daily energy to be supplied. Equations (52) and (53) give respectively maximum power that battery must be able to absorb/deliver, where 'j' varies on monthly basis and 't' varies on hourly basis. The battery must be able to absorb and supply a maximum energy respectively by (54) and (55). The coefficient Sigma (σ) was introduced to take into account only moments of the day where the battery must absorb energy, on the maximum daily energy calculation. Unlike σ , lambda (λ) allows taking into account only moments of the day where the battery must supply energy, in the minimum daily energy calculation. Therefore, these coefficients are given by (56) and (57).

$$P_{bat}^{pchmax} = -\max_{j=1...12} (\max_{t=0...24} (P_{PV}^{MPPT}(t) + P_{wind}^{MPPT}(t) - P_{load}(t) + P_{UG}^{max})) < 0 \quad (52)$$

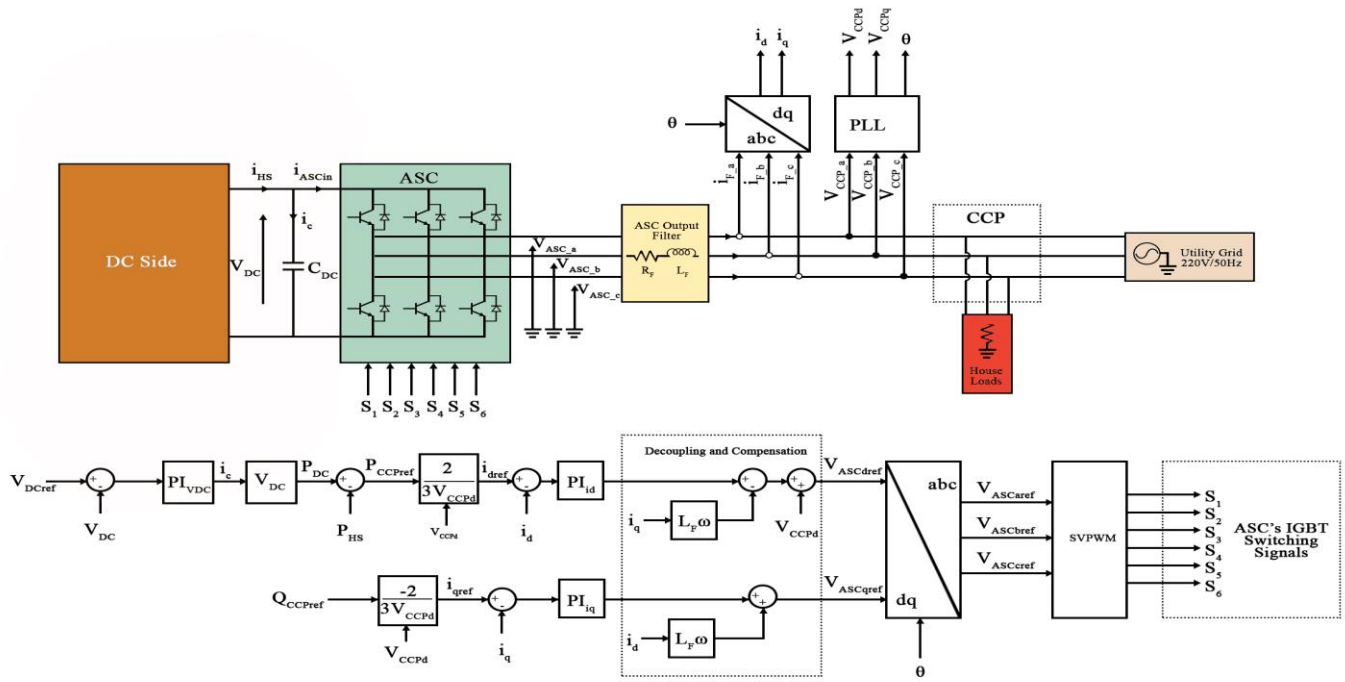


Figure 17: Overall ASC Control Architecture

$$P_{bat}^{dischmax} = -\min_{j=1\dots 12}(\min_{t=0\dots 24}(P_{PV}^{MPPT}(t) + P_{wind}^{MPPT}(t) - P_{load}(t) + P_{UG}^{max})) > 0 \quad (53)$$

$$E_{bat}^{chmax} = -\sum_{t=1}^{24} \sigma(P_{PV}^{MPPT}(t) + P_{wind}^{MPPT}(t) - P_{load}(t) + P_{UG}^{max}) < 0 \quad (54)$$

$$E_{bat}^{dischmax} = -\sum_{t=1}^{24} \lambda(P_{PV}^{MPPT}(t) + P_{wind}^{MPPT}(t) - P_{load}(t) + P_{UG}^{max}) > 0 \quad (55)$$

$$\sigma = 1 \text{ When } P_{PV}^{MPPT}(t) + P_{wind}^{MPPT}(t) - P_{load}(t) + P_{UG}^{max} > 0$$

$$\sigma = 0 \text{ otherwise} \quad (56)$$

$$\lambda = 1 \text{ When } P_{PV}^{MPPT}(t) + P_{wind}^{MPPT}(t) - P_{load}(t) + P_{UG}^{max} < 0$$

$$\lambda = 0 \text{ otherwise} \quad (57)$$

The maximum daily energy that the battery must be able to absorb is around -57.604kWh for the most favorable case of the year, and the maximum daily energy that it must be able to deliver is 40.112kWh for the worst one. Finally, equation (58) gives the Battery capacity.

$$C_{bat} = \frac{\max_{j=1\dots 12}(A, B)}{V_{bat}(SOC_{max} - SOC_{min})} \quad (58)$$

Where:

$$A = \sum_{t=1}^{24} \sigma(P_{PV}^{MPPT}(t) + P_{wind}^{MPPT}(t) - P_{load}(t) + P_{UG}^{max})$$

$$B = |\sum_{t=1}^{24} \lambda(P_{PV}^{MPPT}(t) + P_{wind}^{MPPT}(t) - P_{load}(t) + P_{UG}^{max})|$$

The values of SOC_{min} and SOC_{max} are fixed to 20% and 80% respectively, in order to take advantage of the battery performances without reducing its lifespan. These values correspond to the most often recommended values found in the literature of Lead-Acid batteries technology. Therefore, the maximum depth of discharge $DOD_{max} = SOC_{max} - SOC_{min} = 60\%$, and considering an operating voltage of 504V, the battery capacity is given by (59).

$$C_{bat} = \frac{57.604kWh}{504V \cdot 0.6} = 191Ah \quad (59)$$

In consequence, a 191Ah, 12V battery rating is considered. Hence 42 Batteries are required to connect in series to constitute the battery bank.

B. Proposed Supervisory System

The power flow management within the GCHRES is governed by a supervisory controller through EMSs. As mentioned at the introduction, EMS1 controls the power flow for systems with either reversible or irreversible electromechanical metering with no injection limitation of power into the UG. Like EMS1, EMS2 is destined for systems with the same metering types, but targets the case when the power injection into the UG is limited. EMS 3 is dedicated to digital metering. All these EMSs have as main common purpose to ensure supply reliability and continuity to the AC-load (house), while respecting the battery technical constraints. Hence, they all aim to keep the battery SOC between SOC_{min} and SOC_{max} . To get always operational when requested for peak shaving, the three EMSs aim to charge the battery as soon as possible, using the available energy source; Renewable energy sources (PVG+DFIG) or UG, or both at the same time.

Fig.18 depicts the supervisory controller scheme. Supervisory inputs are related firstly to the type of metering (METERTYPE input), followed by the UG constraints in term of maximum

Injectable power P_{UG}^{injmax} (input Gridlim=1 for injection limitation and Gridlim=0 otherwise), and in term of subscription power P_{UG}^{max} . Battery constraints concern the SOC and maximum charging/discharging powers P_{bat}^{chmax} and $P_{bat}^{dischmax}$ respectively. Power measurement Inputs are the load demand power P_{load} , and the net power P_{net} equal to the difference between RES power (PVG & wind turbine) and load demand $P_{net} = P_{pv} + P_{wind} - P_{load}$. Outputs in terms of battery power reference P_{batref} , PVG power reference P_{pvref} in case of solar power limitation (LimPV=1), and Wind power reference $P_{windref}$ in case of wind power limitation (Limwind=1), are generated by the supervisory controller. PVG system is turned off in some few cases. Choosing to turn off the PVG and not the wind generator is supported by the fact that restarting the wind system is a rather complex manoeuvre than restarting the PVG system. In fact, the system goes through several steps when passing from start to normal operation (feathering of the blades that last 90 seconds after the restarting, wind turbine in slow down operation mode...). The decision of turning On/Off the PVG is given by the supervisory controller by its output "Pvon" (on when Pvon=1 and off when Pvon=0). This output controls the state of the PVG circuit breaker (Fig. 5). When turned on, and when power limitation is not necessary, PVG operates by default under MPPT mode, otherwise it is controlled by mean of LPPT algorithm. Unlike PVG, Wind power source is always operating. It operates by default in MPPT mode, but can be driven to reduce its generated power in certain cases, by the mean of a reduced power control. When there is a need of renewable energy sources production reducing, the three EMSs have as common aim to limit PVG power firstly. In fact, limiting this device power is easier by simple intervention on its output voltage by means of DC/DC Boost converter. Contrarily, wind system is more complex to control, with higher time response due to the system inertia. Fig. 19 represents these proposed EMSs with their different operating modes.

IV. SIMULATION RESULTS AND DISCUSSION

The performances of the proposed GCHRES, supervised by each EMS individually, are tested by means of simulation on MATLAB/SIMULINK, during a whole day of May. Simulation time is 12 Seconds within the logic of assigning a half of a second to each hour. The CGHRES runs through three macro operating modes according to the battery SOC:

- Normal Battery Operating Mode (NBOM): battery SOC is between its recommended limits SOC_{min} and SOC_{max} .
- Very Deep Discharged Battery Operating Mode (VDDBOM): battery SOC is inferior to its lower limit (SOC_{min}). It can occur due to battery self-discharge phenomenon caused by a no use of the battery for a long time.
- Overcharged Battery Operating Mode (OBOM): when battery SOC is higher than its upper limit (SOC_{max})...According to the battery sizing method developed in this paper, $P_{bat}^{chmax} = -6.8kW$ and $P_{bat}^{dischmax} = 5.2kW$, $SOC_{min} = 20\%$ and $SOC_{max} = 80\%$. the subscription power with the UG was fixed at $P_{UG}^{max} = -5kW$, and $P_{UG}^{injmax} = 2kW$. Note that peak hours run from 18h to 23h in May in Morocco. As common results for all EMSs,

the power provided by the grid rarely exceeded $P_{UG}^{max} = -5Kw$ (Fig. 24, Fig. 30 and Fig. 37), especially during peak hours, participating consequently in the grid congestion limitation during these peak time slot. However, sometimes, a little overflow in UG power is necessary to avoid battery maximum discharging power exceeding (leading to no-respect of battery technical constraints that come before UG constraints). The value of the sampling time adopted is $T_s = 10^{-5}$ s. The simulation of Each EMS is divided into time intervals corresponding to the same operating mode. The results in this section will be discussed as follow:

- CGHRES power sharing during (NBOM).
- CGHRES power sharing during (VDDBOM).
- Wind turbine power limitation during (OBOM).
- Overall system results and different devices behavior.

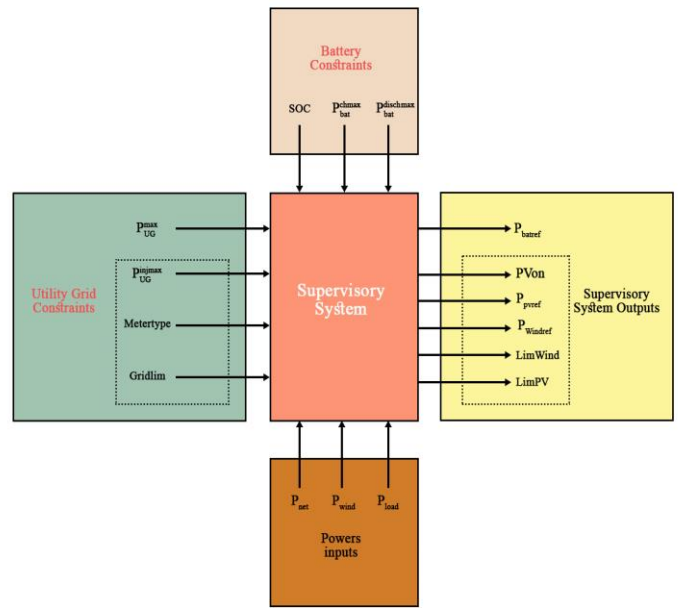


Fig 18: GCHRES supervisory controller scheme

A. Normal Battery Operating Mode (NBOM)

A.1 Energy Management Strategy 1 (EMS 1)

Fig. 20 shows EMS1 operation modes. It shows also that due to the no need of power limitation generation (unlimited power injection into the UG), Limp and Limwind supervisory outputs are always equals to 0, and PVon equals to 1, allowing the two generators to operate in their fully potential (MPPT operation for both). The net power (P_{net}) is shown in Fig. 21 and the system different powers are all shown in Fig. 22. Fig. 23 shows the battery power P_{bat} (negative when charging/ positive when discharging to perform peak shaving function), by following its reference P_{batref} generated according to each mode. This figure shows the respect of this device powers constraints P_{bat}^{chmax} and $P_{bat}^{dischmax}$. UG power (P_{UG}) is shown in Fig. 24. This figure shows that the injection is realized without any limitation. Finally, Fig. 25 presents the battery SOC evolution. The battery begin the simulation with an initial

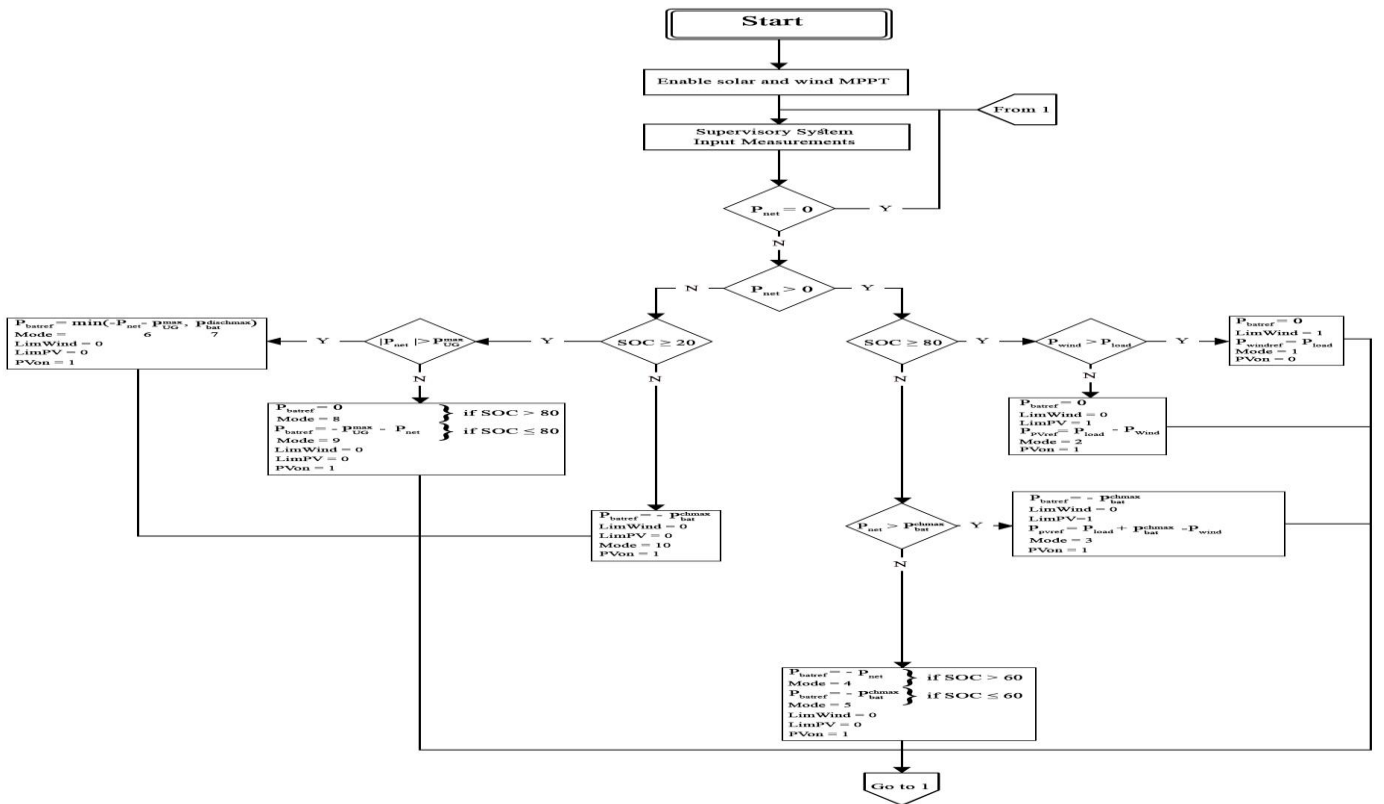
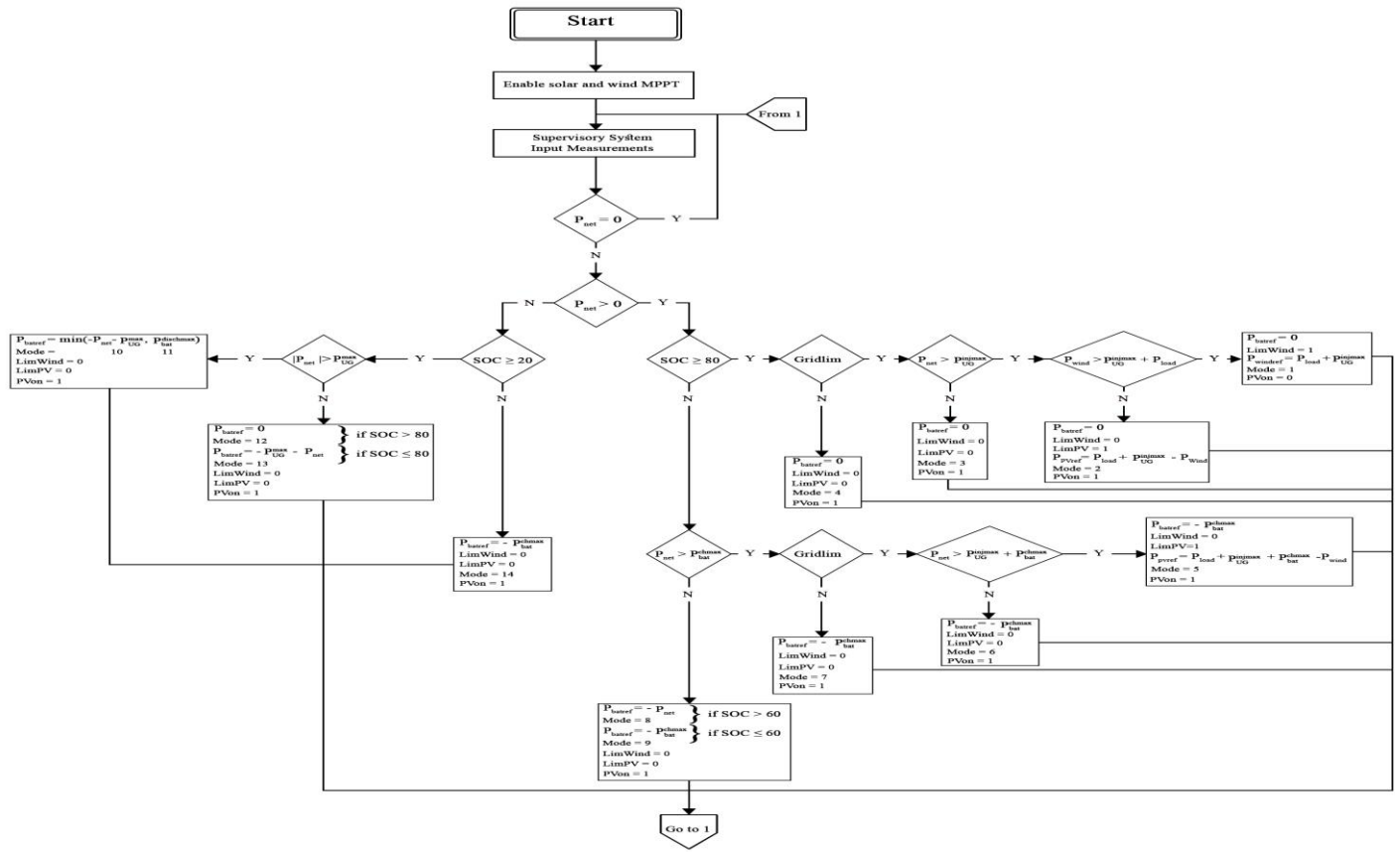


Figure 19: Combined EMS1 and EMS2, and EMS3

$SOC_{t=0s}=56\%$, aiming to make the simulation as realistic as possible (considering its operation during the previous 24 hours). The SOC constraint was respected ($SOC_{min}^{day} = SOC_{t=1.5s} = 46\%$ and $SOC_{max}^{day} = 80\%$ between 6.8sec and 8sec). Thus, the battery had been operational throughout this day and remain sufficiently charged for the next day peak shaving operation ($SOC_{t=12s} = 68\%$).

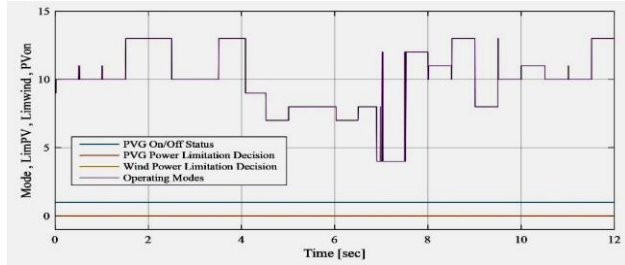


Fig 20: Operating modes, RES limitation decisions and PVG status (EMS 1)

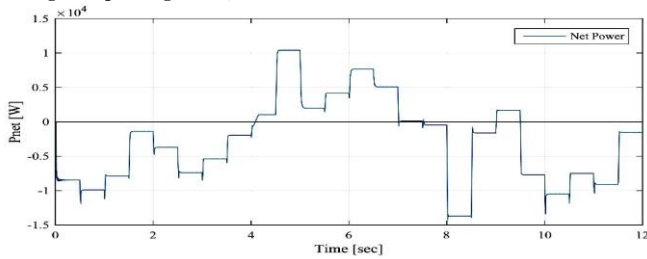


Fig 21: net power (EMS 1)

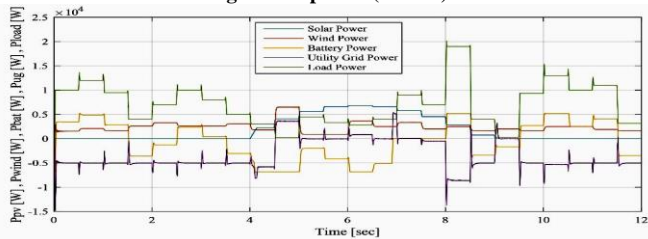


Fig 22: PVG, Wind, battery, UG and load powers (EMS 1)

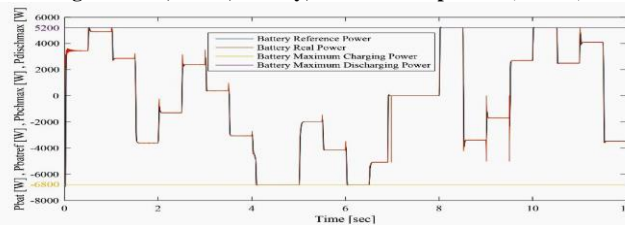


Fig 23: Battery and battery reference powers (EMS 1)

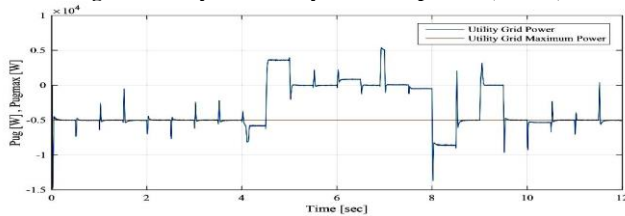


Fig 24: UG power (EMS 1)

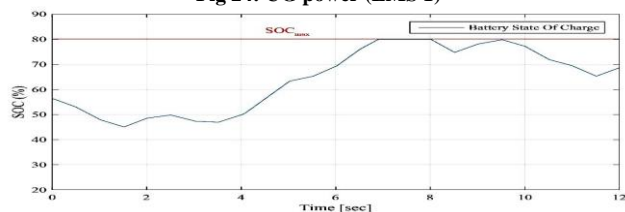


Fig 25: Battery SOC evolution (EMS 1)

A.2 Energy Management Strategy 2 (EMS 2)

Fig. 26 shows EMS2 operation modes. It shows also that PVG and Wind turbine operates by default under their respective MPPT control. However, due to the need of power limitation generation in certain cases (limited power injection into the UG when battery are fully charged $SOC = SOC_{max}$ or when surplus exceeds battery maximum charging power P_{bat}^{chmax}), the PVG is still turned on ($P_{von}=1$) but ($LimPV=1$) to switch toward LPPT control, and PVG output is limited to its reference P_{pvref} as presented in Fig. 31. During NBOM, only PVG is switched to LPPT, because maximum Wind generated power ($P_{DFIG}^{nom} = 6.5kW$) is always inferior to $|P_{bat}^{chmax}| + P_{UG}^{injmax} + P_{load} = 6.8kW + 2kW + P_{load}$. Net power (P_{net}) is shown in Fig. 27. System different powers are shown in Fig. 28. As for EMS1 Fig. 29 shows battery power (P_{bat}) following its references and respecting its powers constraints. UG power (P_{UG}), is shown in Fig. 30. This figure shows that power injection into the UG never exceeds ($P_{UG}^{injmax} = 2kW$). Finally, Fig. 32 presents the battery SOC evolution. As with EMS1, $SOC_{t=0s}=56\%$. The SOC constraint was respected ($SOC_{min}^{day} = SOC_{t=1s} = 52.6\%$ and $SOC_{max}^{day} = 80\%$ between 6.5sec and 8sec and between 9sec and 9.5sec). Thus, the battery had been operational throughout this day and remain sufficiently charged for the next day ($SOC_{t=12s} = 75.5\%$).

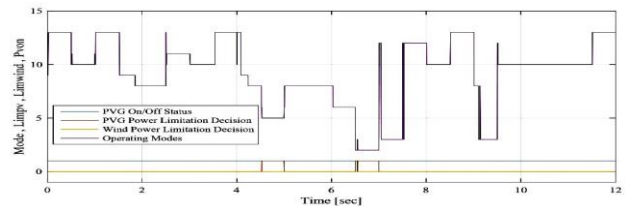


Fig 26: Operating modes, RES limitation decisions and PVG status (EMS 2)

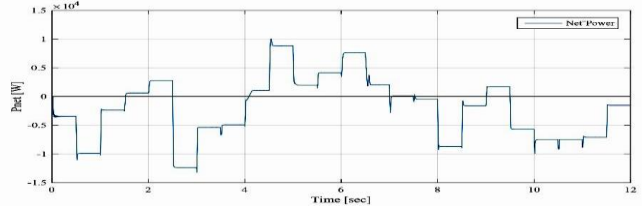


Fig 27: net power (EMS 2)

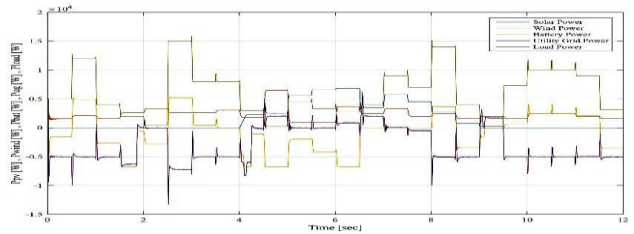


Fig 28: PVG, wind, battery, UG and load powers (EMS 2)

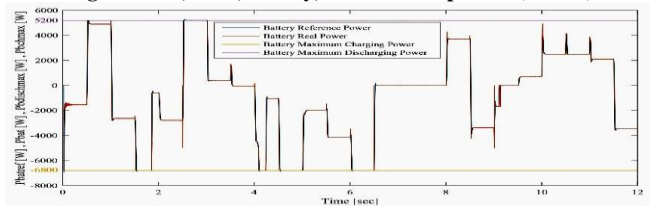


Fig 29: Battery and battery reference powers (EMS 2)

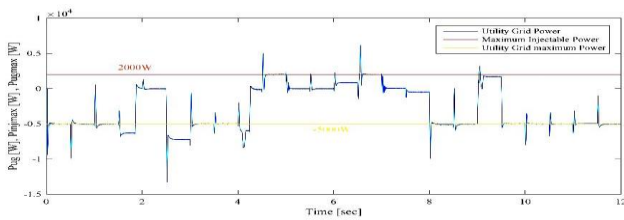


Fig 30: UG power (EMS 2)

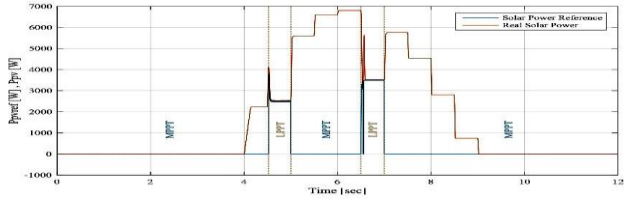


Fig 31: PVG and PVG reference powers (EMS 2)

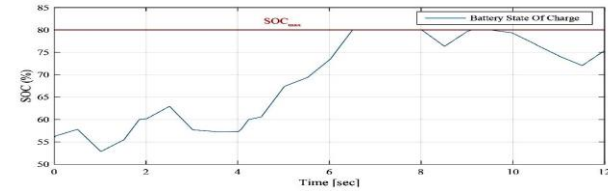


Fig 32: Battery SOC evolution (EMS 2)

A.3 Energy Management Strategy 3 (EMS 3)

Same results as EMS1 are presented respectively in Fig. 33, Fig. 34, Fig. 35, Fig. 36, Fig. 37 and Fig. 38. Fig. 36 and Fig. 38 show that battery SOC and powers constraints were all respected. UG power (P_{UG}), is shown in Fig. 37 and shows that zero power was injected into the UG ($P_{UG}^{in,max} = 0kW$). As with precedent EMSs, $SOC_{t=0s} = 56\%$. SOC constraint was respected ($SOC_{min}^{day} = SOC_{t=4s} = 37.5\%$ and $SOC_{max}^{day} = 80\%$ between 7.6sec and 9.2sec). Thus, the battery had been operational throughout this day and remain sufficiently charged for the next day ($SOC_{t=12s} = 64\%$). PVG and Wind turbine had the same behavior as for EMS2, with a difference on the PVG power reference level P_{pvref} (and wind turbine always in MPPT mode). Therefore, there is no need to show PVG power with its reference, because it has been discussed in EMS2 results. The operating modes 10, 9, 8, 7 and 6 are similar to the ones related to EMS1 and EMS2 because all proposed EMSs have the same left part of the flowchart (when $P_{net} < 0$ in Fig. 19).

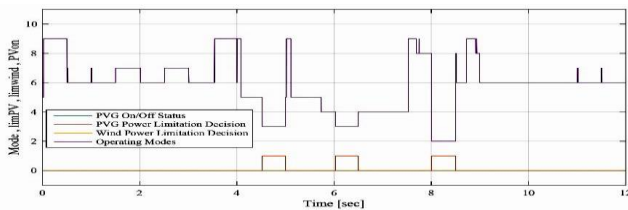


Fig 33: Operating modes, RES limitation decisions and PVG status (EMS 3)

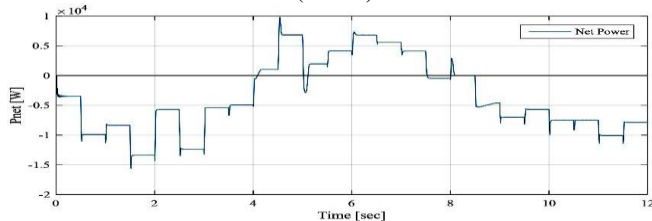


Fig 34: net power (EMS 3)

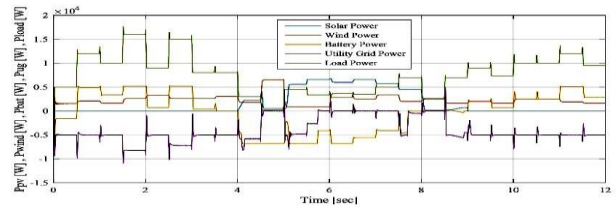


Fig 35: PVG, wind, battery, UG and load powers (EMS 3)

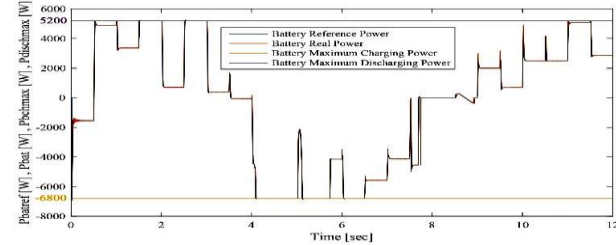


Fig 36: Battery and battery reference powers (EMS 3)

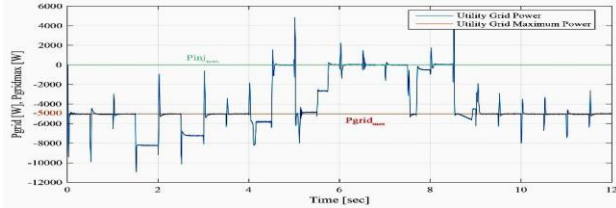


Fig 37: UG power (EMS 3)

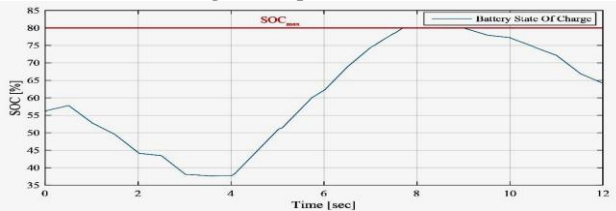


Fig 38: Battery SOC evolution (EMS 3)

B. Very Deep Discharged Battery Operating Mode (VDBOM)

This mode corresponds to the common and last mode of all EMS and will be simulated only once for all EMSs. Fig. 39 shows the SOC which starts with a value equals to 17% which is lower than $SOC_{min} = 20\%$. This figure shows that SOC is rapidly increasing due to battery charging via ($P_{bat}^{ch,max}$), until it reaches (SOC_{min}). Fig. 40 shows the power sharing within the CGHRES. After 0.12 (transient period), this figure shows that even if ($P_{net} < 0$), the UG provides a power which is largely higher than the subscription power (P_{UG}^{max}), to charge battery faster avoiding harming it due to its deep discharge (technical constraints of the battery comes before grid constraints). Indeed, RES generators operate according to their respective MPPT control.

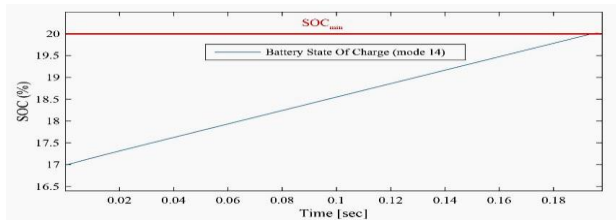


Fig 39: Battery SOC evolution in VDBOM (for all EMSs)

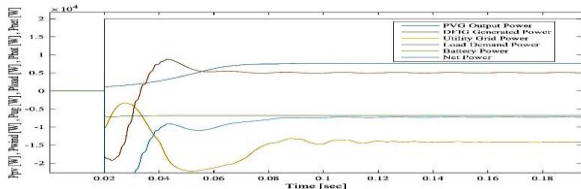


Fig 40: PVG, wind, battery, UG and load powers in VDDBOM (for all EMSs)

C. Wind Turbine Power Limitation in OBOM

Mode 1 is similar for the two EMS2 and EMS3, and differ only in the wind power reference ($P_{windref}$) generated by each EMS. Consequently, only one case will be discussed and will explain the behaviour of both EMSs during this mode. This latter correspond to an over RES power generation, that must be limited (battery overcharged, no power injection into UG for EMS3, power injection limitation for EMS2...). The wind generation alone can satisfy the demand ($P_{wind} > P_{load}$). Therefore, the PVG must be turned off ($PV_{on}=0$), and P_{wind} limited to ($P_{windref}=4kW$) between 0.6s and 2.4s (output supervisory $Lim_{wind}=1$) as shown in Fig. 41, which corresponds to the reduced power operation of the wind turbine. Fig. 42 shows the decrease of the power coefficient ($C_p(\lambda_{lim}, 0) = 0.32 < C_{pmax} = 0.5$), and the corresponding TSR (λ_{lim}) is lower than the optimal TSR ($\lambda_{lim} = 3.5 < \lambda_{opt} = 9.2$) as shown in Fig. 43. It is seen that the time response of the switching from MPPT to the reduced power of the wind turbine (around 1 second of transient), is higher than the one concerning the PVG system (Fig. 31), due to DFIG rotor inertia, which support the said above choice of reducing PVG power system firstly, and if necessary, reducing wind turbine generation secondly.

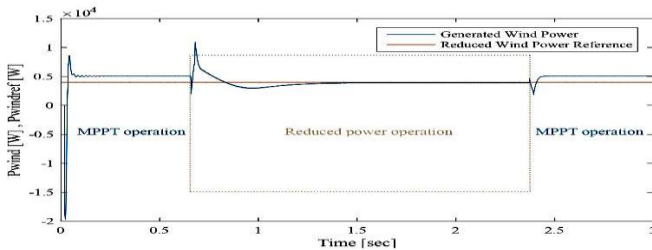


Fig 41: reduced power mode of wind turbine

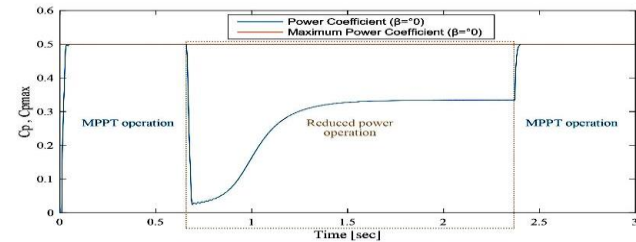


Fig 42: reduced power coefficient of the wind turbine

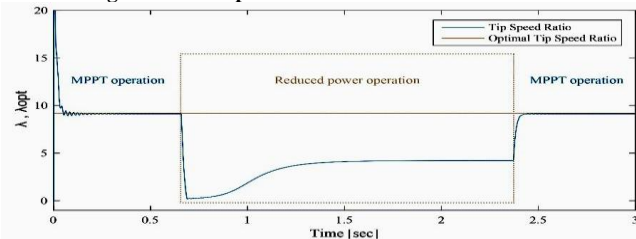


Fig 43: TSR corresponding to wind turbine reduced power mode

D. Overall system results & devices control performances

Performances of the different devices control of the CGHRES supervised by EMS2 are discussed. The system presents the same performances when supervised through EMS1 and EMS3. Regarding PVG system, Fig. 44 and Fig. 45 show respectively PVG output current (I_{pv}) and voltage (V_{pv}), showing also the MPPT and the LPPT control region. Fig. 45 indicates that when PVG is controlled via LPPT algorithm, the LPP is reached by imposing the greater of the two possible voltages.

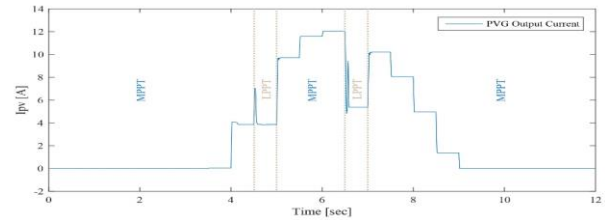


Fig 44: PVG output current (EMS2)

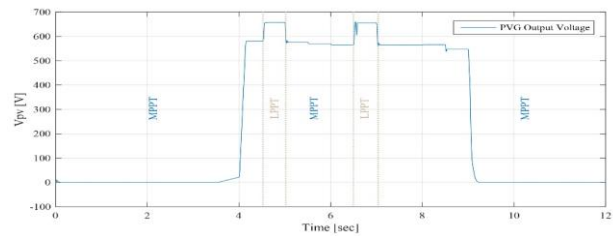


Fig 45: PVG output voltage (EMS2)

Fig. 46 shows that while Wind system is operating under MPPT control, even if the wind speed change, the power coefficient is always maintained on its maximal value for a pitch angle equals to zero ($C_p(\lambda_{opt}, 0) = C_{pmax} = 0.5$). This occurs by adapting the TSR to its optimal value ($\lambda = \lambda_{opt} = 9.2$) as shown in Fig. 47. This adaptation is realized by following MPPT electromagnetic torque reference depicted in Fig. 48.

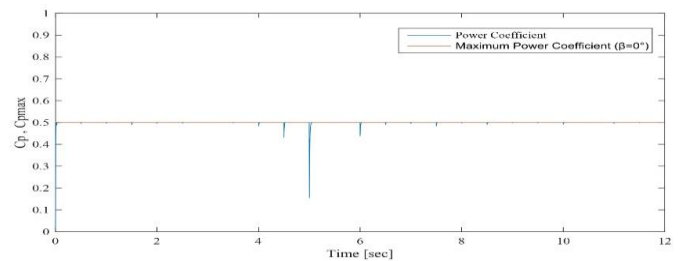


Fig 46: Power coefficient under MPPT mode

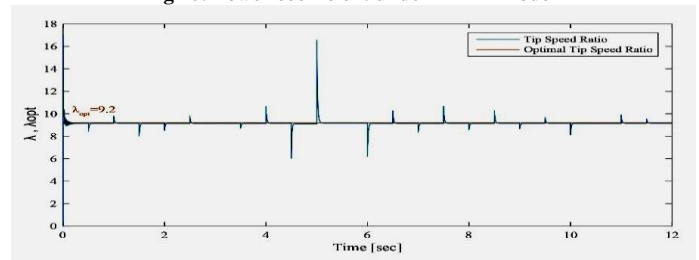


Fig 47: Optimal TSR for MPPT mode

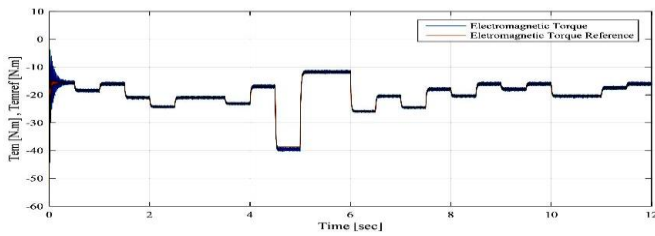


Fig 48: Electromagnetic torque vs. reference under MPPT mode

Fig. 49 shows that the rotor direct current follows its reference fixed to zero ($I_d = I_{dref} = 0$) as presented in DFIG control section.

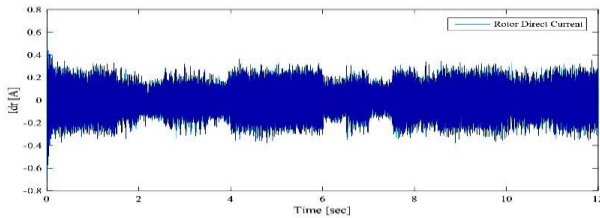


Fig 49: DFIG rotor direct current

Fig. 50 and Fig. 51 shows respectively stator and rotor currents of the DFIG. It is clear that the frequency of the stator currents is constant and equals to 50Hz. contrarily, rotor currents frequency is variable, because the DFIG speed is PWM controlled through its rotor via the RSC.

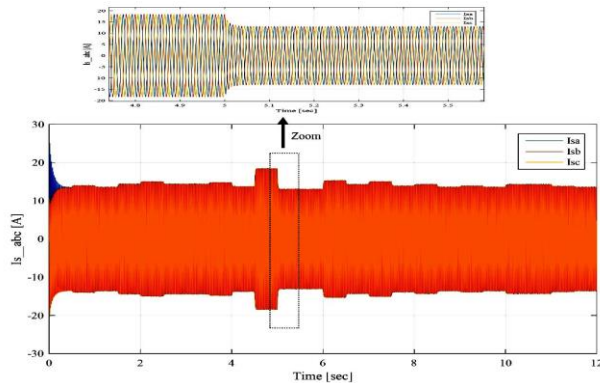


Fig 50: DFIG stator currents

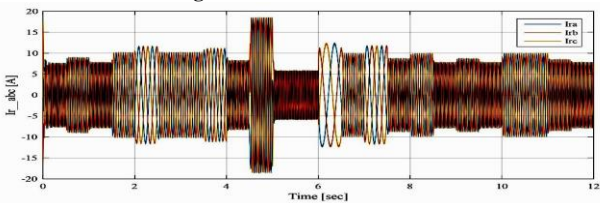


Fig 51: DFIG rotor currents

Fig. 52 shows stator and rotor power of the DFIG, while Fig. 53 shows the speed of the DFIG (electrical speed) for every wind speed. According to these two figures, it can be seen that stator power is continuously sent to the CCP ($P_s < 0$), while the rotor power can be sent to the CCP ($P_r < 0$ in Hyper-synchronous mode when DFIG speed is higher than the synchronism speed equal to 157.09rad/s), and this power is absorbed by the rotor ($P_r > 0$ in Sub-synchronous mode when DFIG speed is less than the synchronism speed). Fig. 53 shows also that the speed of the DFIG is always in the speed variation range

corresponding to $[-35\%, +35\%]$ of the synchronism speed which is $[102\text{rad/s}, 212\text{rad.s}]$.

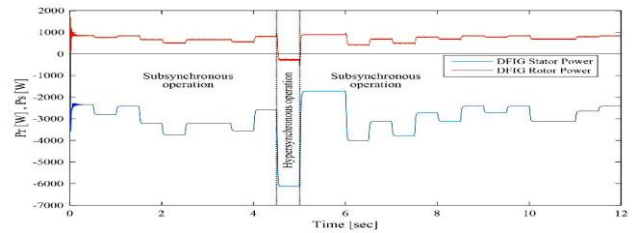


Fig 52: DFIG stator and rotor powers

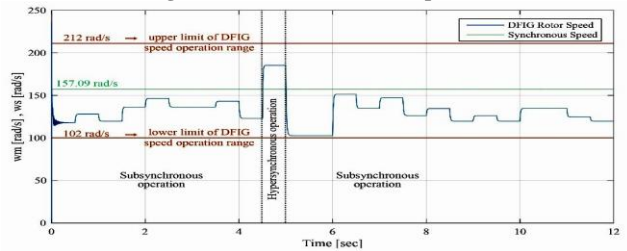


Fig 53: DFIG electrical speed

It is shown in Fig. 54 that the real power into the overall GCHRES is equals to zero. It proves the performances of the system in term of power quality and stability. In fact, the line to line voltage of the load is altered if the overall system contains real power [34]. The DC- bus voltage is inside standard limits as shown in Fig. 55 [35]. Fig. 56 depicts that there is no reactive power exchange between the CCP and the ASC.

It should be noticed that the transients present in some figures, are due to the loads switching via circuit breakers in MATLAB/SIMULINK, and last no longer than tenth of second, which is negligible in the case of the real operation of the system throughout the 24 hours of the day.

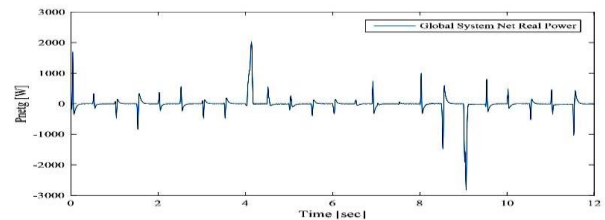


Fig 54: Overall system real power

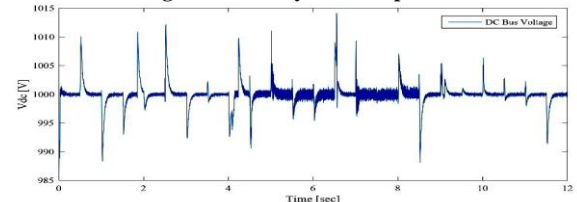


Fig 55: DC-Bus voltage

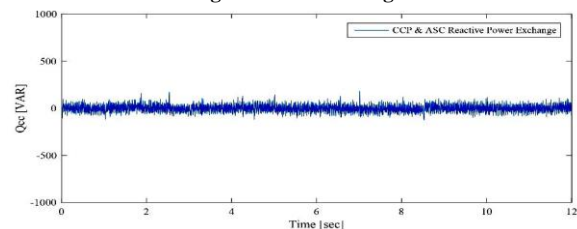


Fig 56: Reactive power exchange between ASC and CCP

V. CONCLUSION

Three novels energy management strategies, supervising and controlling the power flows within a GCHRES were proposed in this paper. These EMSs differ depending on the UG metering types. Their common purpose was to ensure power supply reliability of the load variable demand through the whole day’s 24 Hours. These EMSs aim also to preserve battery internal circuit and consequently avoiding its lifespan reducing. In addition, reducing the monthly energy bill of the UG subscriber through battery peak shaving application, was a common purpose. The dynamic behaviours of the proposed GCHRES, supervised by each one of these EMSs, were tested under variable load demand profiles and real weather data of the region of Marrakech/Morocco. The effectiveness of the GCHRES in terms of house demand meeting, overall system stability, DC-Bus voltage regulation, power quality, reliability of power supply and element constraints (battery/UG) respecting, was confirmed via simulation in MATLAB/SIMULINK.

APPENDIX A

Fig. A.1 (a) depict real average solar irradiation, and **Fig.A.1 (b)** shows the average temperature data of the region of Marrakech, while **Fig. A.2** shows the average wind speed of this region, modified a little for simulation purpose. These data were collected on hourly basis. **Tab. A.1** shows the site localization and also the data base information for solar system.

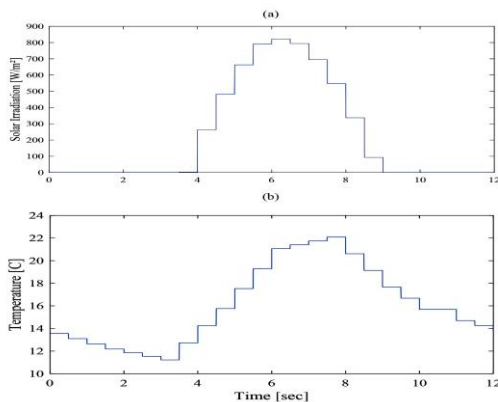


Fig. A.1: Real Weather data (a) average solar irradiation (b) average temperature (May-Marrakech)

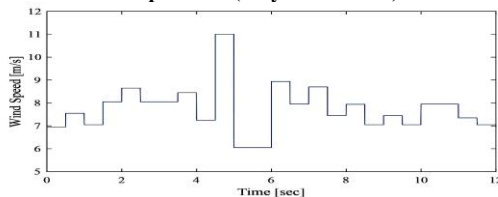


Fig. A.2: Wind Speed (May-Marrakech)

Tab. A.1: Real solar irradiation and temperature data

Data base	PVGIS-SARAH
Region	Marrakech / Morocco
Latitude / Longitude	31,627 / - 7,988
Month	May
Horizon	calculated
Irradiation	Fixed orientation /Tilt 30°/Azimuth 0°

CONFLICT OF INTEREST

The authors declare no conflict of interest.

REFERENCES

- [1] Gomez, L.A.G., Grilo, A.P., Salles M.B.C., & Filho, A.J.S. (2020). Combined Control of DFIG-Based Wind Turbine and Battery Energy Storage System for Frequency Response in Microgrids. *Energies*, 12(4).
- [2] Hussein, K. H., Muta, I., Hshino, T., & Osakada, M. (January 1995). Maximum photovoltaic power tracking: an algorithm for rapidly changing atmospheric conditions. *IEE Proceedings -Generation, Transmission and Distribution*, 142(1), 59-64.
- [3] Wu, T., Chang, C., & Chen, Y. (April 2000). A fuzzy -logic controlled single -stage converter for PV-powered lighting system application. *IEEE Transactions on Industrial Electronics*, 47(2), 287-296.
- [4] Zhang, C., Zhao, D., Wang, J., & Chen, G. (2009). A modified MPPT method with variable perturbation step for photovoltaic system. *IEEE 6th International Power Electronics and Motion Control Conference*, 2096-2099.
- [5] Faranda, R., Leva, S., & Maugeri, V. (2008). MPPT techniques for PV systems: energetic and cost comparison. *IEEE Power and Energy Society General Meeting – Conversion and Delivery of Electrical Energy in the 21st Century*.
- [6] Dharif, M. (2016). Modélisation de l’intégration de l’énergie photovoltaïque au réseau électrique national. *Doctoral thesis, Cadi Ayad University- Sciences and Technology faculty of Marrakech*.
- [7] Go, S. I., Ahn, S. J., Choi, J. H., Jung, W. W., Yun, S. Y., & Song, I. K. (2011). Simulation and Analysis of Existing MPPT Control Methods in a PV Generation System. *Journal of International Council on Electrical Engineering*, 1(4), 446-451.
- [8] Femia, N., Petrone, G., Spagnuolo, G., & M. Vitelli, M. (2004). Optimizing sampling rate of P&O MPPT technique. *IEEE 35th Annual Power Electronics Specialists Conference*, 1945-1949.
- [9] Liu, X., & Lopez, L. A. C. (2004). An improved perturbation and observation maximum power point tracking algorithm for PV arrays. *IEEE 35th Annual Power Electronics Specialists Conference*, 1945-1949.
- [10] Lawrence, K. L., Josiah, L. M. & Yskandar, H. (2014). Dynamic performance analysis of an integrated wind/photovoltaic microgrid with storage. *International Journal of Smart Grid and Clean Energy*, 3(3), 307-317.
- [11] Thiringer, T., & Linders, J. (1993). Control by variable rotor speed of a fixed pitch wind turbine operating in a wide speed range, *IEEE Transactions on Energy Conversion*, 8(3), 520-526.
- [12] Chinchilla, M., Arnaltes, S., & Burgos, J. C. (2006). Control of permanent magnet generators applied to variable-speed wind-energy systems connected to the grid. *IEEE Transactions on Energy Conversion*, 21(1), 130-135.
- [13] Ermis, M., Ertan, H. B., Akpinar, E., & Ulgut, F. (1992). Autonomous wind energy conversion systems with a simple controller for maximum power transfer. *Proc. Inst. Elect. Eng. B*, 139(5), 421-428.

- [14] Tan, K., & Islam, S. (2004). Optimum control strategies in energy conversion of PMSG wind turbine system without mechanical sensors. *IEEE Transactions on Energy Conversion*, 19(2), 392-399.
- [15] Onar, O. C., Uzunoglu, M., & Alam, M. S. (2006). Dynamic modeling, design and simulation of a wind/fuel cell/ultra-capacitor-based hybrid power generation system. *J. Power Sources*, 161(1), 707-722.
- [16] Bennouna, A. (2020). Autoproduction d'électricité-Pour qui est fait le Projet de Loi en gestation?. *chantiers du maroc*, <https://chantiersdumaroc.ma/btp-qui-bouge/dossiers/autoproduction-delectricite-renouvelable-la-loi-en-gestation/>.
- [17] European Parliament. (2008). Outlook of Energy Storage Technologies, *European Parliament's committee on Industry, Research and Energy (ITRE)*, IP/A/ITRE/FWC/2006-087/Lot 4/C1/SC2, http://www.storiesproject.eu/docs/study_energy_storage_final.pdf.
- [18] Riffonneau, Y. (2009). Gestion des flux énergétiques dans un système photovoltaïque avec stockage connecté au réseau. *Doctoral Thesis, Grenoble Alpes University*.
- [19] Bennouna, A. (2020). Produire son électricité solaire au Maroc, c'est possible et peut être rentable... malgré tout !. *EcoActu*. <https://www.ecoactu.ma/produire-son-electricite-solaire/>.
- [20] Guichi, A., Talha, A., Berkouk, E. M., & Mekhilef, S. (2018). Energy Management and Performance Evaluation of Grid Connected PV-Battery Hybrid System with Inherent Control Scheme. *Sustainable Cities and Society*, Vol. 41.
- [21] Kiran, P. B. S. (2015). Limited Power Control of a Grid Connected Photovoltaic System. *Master Thesis, Indian Institute of Technology Gandhinagar*.
- [22] Bouharchouch, A., Berkouk, E. M., & Ghennam, T. (2013). Control and Energy Management of a Grid Connected Hybrid Energy System PV-Wind with Battery Energy Storage for Residential Applications. *Eighth International Conference and Exhibition on Ecological Vehicle and Renewable Energies (EVER)*.
- [23] Lachguer, N. (2015). Gestion optimale des flux de puissance et amélioration de la qualité d'énergie des systèmes éoliens à base des machines: -Asynchrone à double alimentation. -Synchrone à aimants permanents. *Doctoral Thesis, Semlalia Sciences University of Marrakech*.
- [24] Abad, G., Lopez, J., Rodriguez, M. A., Marroy, L., & Iwanski, G. (2011). Introduction to a Wind Energy Generation System. *Doubly Fed Induction Generator Modeling and Control for Wind Energy Generation*, 1st ed., Published by John Wiley and Sons Inc., Hoboken, New Jersey, 1-85.
- [25] Abad, G., & Iwanski, G. (2014). Properties and Control of a Doubly Fed Induction Machine. *Power Electronic for Renewable Energy Systems Transportation and Industrial Applications*, 1st ed., vol. 3, Ltd. Published by John Wiley and Sons, 271-317.
- [26] Labbé, J., (2006). L'hydrogène électrolytique comme moyen de stockage d'électricité pour systèmes photovoltaïques isolés. *Doctoral thesis, Paris Mining School*.
- [27] Dekkiche, A. (2008). Modèle de batterie générique et estimation de l'état de charge. *Master Thesis in Electronic, Superior Technology School, Quebec University*.
- [28] Tremblay, O., Dessaint, L. A., & Dekkiche, A. I. (2007). A Generic Battery Model for the Dynamic Simulation of Hybrid Electric Vehicles. *IEEE Vehicle Power and Propulsion Conference*, 284-289.
- [29] Jackey, R. A. (2007). A simple, Effective Lead-Acid Battery Modelling Process for Electrical System Component Selection, *SAE International*.
- [30] Ceraolo, M. (2000). New dynamical models of Lead-Acid batteries, *IEEE Transactions on Powers Systems*, 15(4), 1184-1190.
- [31] SimPowerSystems TM Reference, Hydro-Québec/the Math Workds, Inc, Natick, MA, 2010.
- [32] European Commission website "ec.europa.eu", European Commission > EU Sciences Hub > PVGIS > Outils Interactifs, latest update 15 October 2019, https://re.jrc.ec.europa.eu/pvg_tools/fr/#MR.
- [33] https://www.meteoblue.com/fr/meteo/historyclimate/climatemodelled/marrakech_maroc_2542997
- [34] Tariq, K., & Zulqadar, H. S. (2016). Energy Management simulation of Photovoltaic/Hydrogen/Battery Hybrid Power System. *Advances in Science, Technology and Engineering Systems Journal*, 1(2), 11-18.
- [35] "IEEE Standard for Interconnecting Distributed Resources with Electric Power Systems", *IEEE Std 1547-2003*, 2003.